

A fast spatio-temporal temperature predictor for vacuum assisted resin infusion molding process based on deep machine learning modeling

Runyu Zhang¹ · Yingjian Liu¹ · Thomas Zheng² · Sarah Eddin³ · Steven Nolet⁴ · Yi-Ling Liang⁵ · Shaghayegh Rezazadeh⁴ · Joseph Wilson⁴ · Hongbing Lu¹ · Dong Qian¹

Received: 14 October 2022 / Accepted: 9 March 2023 © The Author(s), under exclusive licence to Springer Science+Business Media, LLC, part of Springer Nature 2023

Abstract

The manufacture of large wind turbine blades requires well-controlled processing conditions to prevent defect formation and thus produce high-quality composite blades. While the physics-based models provide accurate computational capabilities for the resin infusion and curing process for the glass fiber composites, they suffer from high computational costs, making them infeasible for fast optimization computation and process control during manufacturing. In light of the limitations, we describe a machine learning (ML) approach that employs a deep convolutional and recurrent neural network model to predict the spatio-temporal temperature distribution during the vacuum assisted resin infusion molding (VARIM) process. The ML model is trained with the "big data" generated from the physics-based high-fidelity simulations. Once fully trained, it serves as a digital twin of the blade manufacturing process. Validation is made by comparing simulation results with experimental data on a unidirectional glass fiber composite laminate plate (44 plies, 2 m long and 0.5 m wide). The trained and validated ML model is then extended to evaluate the role of critical VARIM processing parameters on temperature distribution. With the predictive accuracy of 94%, at over 100 times faster computational speed than the physics-based simulations, the ML approach established herein provides a general framework for a digital twin for temperature distribution in the composite manufacturing process.

Keywords Vacuum assisted resin infusion molding (VARIM) \cdot Machine learning (ML) \cdot Deep convolutional neural network (CNN) \cdot Recurrent neural network (RNN) \cdot Long short-term memory (LSTM) \cdot Physics-informed surrogate model

Introduction

In the past few decades, significant efforts have been made in the design and manufacture of large-scale wind turbine blades with increasing efficiency and energy production

Runyu Zhang and Yingjian Liu have contributed equally.

- Center for Wind Energy, Mechanical Engineering, The University of Texas at Dallas, Richardson, TX, USA
- Computer Science and Engineering, Texas A&M University, College Station, TX, USA
- Mechanical Engineering, The University of North Carolina at Charlotte, Charlotte, NC, USA
- 4 TPI Composites, Inc., Warren, RI, USA
- OlinTM EPOXY, Angleton, TX, USA

Published online: 12 May 2023

capacity. The blade spans increase continuously with time, and are projected to reach 120-150 m or longer in the near future (Cotrell et al., 2006; Department of Energy, 2022; Griffith & Ashwill, 2011). Glass fiber-reinforced polymers (GFRP) are often used as the primary structural material in wind blades due to a combination of properties including corrosion-resistance, high strength-to-weight ratio and high stiffness, and low costs. GFRP manufacturing requires impregnating glass fibers with a polymer matrix such as epoxy. The most prevalent method in manufacturing long wind turbine blades is vacuum-assisted resin infusion molding (VARIM) (Hsiao & Heider, 2012), a process that includes applying vacuum/pressure, epoxy resin infusion to fill the highly permeable medium (Hsiao et al., 2000), mold filling (Sun et al., 1998), and heating to properly cure the polymer matrix under thermomechanical conditions (Matsuzaki et al., 2011). It is the goal of blade manufacturers to manufacture



large composite parts without defects. Efforts on controlling the VARIM process have been made in the past, on the flow rate control (Bender et al., 2006; Nalla et al., 2007), post-filling flow monitoring (Simacek et al., 2009, 2012), and controlling other process conditions, such as resin inlet and outlet pressure control, and mold temperature control (Kedari et al., 2011). It is noted that under- and over-heating can introduce inadequate curing and chemical degradation. respectively (Wisnom et al., 2006), and that defects such as high residual stress, and micro-buckling fiber tows can form due to improper processing conditions, which lead to significant delamination (Upadhyaya et al., 2013), reduced compressive strengths, and fatigue life (Fu & Yao, 2022; Samborsky et al., 2010). To date, however, defects such as thermal waves are still often formed in long blades, and as such, defective blades are scrapped, leading to an increase in blade costs. Under such a situation, for each new blade design with a material system, it takes years of effort for wind turbine blade manufacturers to refine their process protocols to produce blades with minimum defects.

Understanding the thermomechanical process in VARIM and their role on stresses, strains, displacements, and temperature distributions, and implementation of a fast high-fidelity digital twin for the manufacturing process for process control can potentially allow operators to take actions in time during the VARIM process to reduce or prevent defect formations. To date, however, multi-physics based simulations take a long time (hours to days, or even longer) to run. The lengthy computation times prevent the use of physics-based models for real-time process control. As the first step towards developing process control, rapid modeling methods and predictive tools are sought after for temperature distribution as a function of time, so that they can be implemented for the control of infusion and curing cycle for composite blades to prevent defect formation.

Modeling the VARIM and the epoxy resin curing processes, in particular, spatio-temporal temperature distribution due to the resin reaction and related heat transfer (Chiu et al., 2000; Struzziero & Teuwen, 2019), and their effects on defect formation (Potter, 2009), such as chemical, thermal, and cure shrinkage (Ersoy & Tugutlu, 2010; Kravchenko et al., 2014), represent a critical challenge due to the coupling of the thermo-chemo-mechanical behavior associated with the curing kinetics (Zhongliang et al., 2019) and thermofluidic-solid response (Ouahbi et al., 2007). Numerous efforts have been made in the past to address the challenges using physics-based simulations (Shojaei et al., 2003), including implementation of non-isothermal simulations of the resin transfer molding process (Mal et al., 1998), modeling of the resin infusion and cure processes in large composites with validations (Ma et al., 2017), and simulations of the resin infusion process considering the compaction and relaxation

of the fabric laminate in the dry and wet state. (Govignon et al., 2008).

Once a validated high-fidelity multiphysics simulation methodology is established, it becomes possible to develop predictive tools, or "digital twins", of the VARIM process. In a digital twin of the VARIM, it takes all inputs including composite layup (ply orientations, etc.), geometry, process conditions (vacuum pressure, mold temperature), and material properties of the fibers and matrix (viscosity, modulus, permeability, shrinkage as a function of degree of cure). Based on these inputs, the digital twin will provide predictive capabilities on a variety of manufacturing outcomes, including resin flow front measurements (Mathuw et al., 2001), the irregular resin flows identification in small channels inside the composite layup (also known as the race-tracking phenomenon) (Devillard et al., 2005; Siddig et al., 2018); filling stage prediction with real-time uncertainty estimation (Tifkitsis & Skordos, 2020); resin flow forecasting using flow control scheme (Matsuzaki et al., 2013), and feedback control loop based on finite difference methods (Nielsen & Pitchumani, 2002); composite structural health monitoring using optical fibers with fiber Bragg gratings for VARIM (Eum et al., 2007); and process-induced void formation prediction in the composite parts using numerical methods (Barari et al., 2019).

The multiphysics models are validated from experimental results, including at times big data collected from different sources, such as wireless sensors under very-high temperatures (Nicolay et al., 2017), and also thermocouple data obtained from a local wireless network (Arnold et al., 2015), towards smart manufacturing (Kusiak, 2017a, 2017b), to establish a digital twin for rapid predictions (Tao et al., 2018). It is noted that these sensors in general provide only limited data, they cannot provide the full field data needed for training a robust data-driven model. In this context, experimentally validated simulation models are capable of bridging this gap by integrating physics-based models with datadriven/machine learning (ML) tools for process modeling and optimization. This integration is crucial as the physicsbased models are known to be accurate after validation and provide high spatio-temporal resolution, but not feasible for predicting in real-time the effects of the multi-physics process of the composite curing.

With advances in powerful computational tools and computer algorithms, the potential of applying artificial intelligence (AI) and ML-driven approaches in many fields to solve complicated tasks is within reach. For instance, researchers have created a powerful machine learning model, named AlphaFold, to accurately predict over 200 million three-dimensional protein structures with atomic accuracy (Jumper et al., 2021), bridging the gap between the incapable physics-based computational methods and the dire need for understanding the function of proteins based on the



protein structure. In other challenging domains, a deep neural network-based AI model that learns from human expert moves, AlphaGo, becomes the first computer program to defeat the best professional human player of the board game Go (Silver et al., 2016), which is thought as one of the most complex strategy board game due to up to 250¹⁵⁰ possible moves. In addition, its improved version, AlphaGo Zero, the AI model that is solely based on the reinforcement learning algorithm (Kaelbling et al., 1996; Mnih et al., 2013; Sutton & Barto, 2018), and trained without human data, has achieved an even more overwhelming victory record of 100–0 defeating its previous version (Silver et al., 2017). Another AI model that is also based on powerful deep reinforcement learning algorithms with mixed-scenario enables real-time control policy-making such that the model defeats the best human e-sports drivers in the PlayStation game Gran Turismo (Wurman et al., 2022), a racing simulation video game with highly complex multi-agent interactions. With newly developed ML algorithms, and integrations of different neural network architectures into the large AI model, which is trained on the enormous and continuously increasing database, many more AI tools become available, such as DALL-E (Ramesh et al., 2021), that can create pictures from language inputs; chatGPT (OpenAI, 2022), that is capable of having human-like conversations through creating the text and code; and finally, GATO (Reed et al., 2022), a generalized agent that is capable of performing all tasks mentioned above.

In the AI applications in the manufacturing sector, deep neural network-based surrogate models have been implemented to optimize the composite textile draping process (Pfrommer et al., 2018), optimizing the resin flow distribution by training a deep neural network using 3D finite element (Szarski & Chauhan, 2023), and predict the production progress in Industrial Internet of Things (IIoT) in manufacturing using a convolutional neural network (CNN)long short-term memory (LSTM) based transfer learning system (Liu et al., 2022). In addition, in polymer composite processing and manufacturing, many studies are devoted to incorporating artificial neural networks (ANN) (Zhang & Friedrich, 2003), and other ML methods to account for defects detection using ultrasonic signal classification and imaging processing techniques (Meng et al., 2017), automated visual detection of geometrical defects (Djavadifar et al., 2021), predictions of cure kinetics parameters (Goli et al., 2020), and mechanical properties (Zhou et al., 2021). In predicting the spatio-temporal temperature distribution in manufacturing composite parts, Amini Niaki et al. developed a physics-informed neural network to simulate the temperature of composite materials under curing based on the thermochemical evolution due to exothermic heat transfer (Amini Niaki et al., 2021), however, the temperature prediction is only one-dimensional, and does not utilize the large data available that can be potentially learned from. To the best of our knowledge, there has not been a comprehensive and easy-to-adapt model for fast, full-field, spatially, and temporally coupled temperature prediction for the VARIM process.

Despite the significant progress made thus far, physics-based predictive tools for the VARIM process still have a critical shortcoming—lengthy computational time—that prevents them from implementation in extensive design optimization analysis, and real-time process controls. To circumvent this limitation, an attempt is made in this work to use machine learning to train the "big data" to develop a fast digital twin. In light of the high expenses required to conduct VARIM experiments which provide only limited experimental data, we use validated multiphysics simulations to generate a large dataset to train the neural network-based digital twin.

Multiple steps are taken in this study to achieve the objectives, including firstly, designing and conducting a lab-scale VARIM experiment based on existing works and inputs from industry collaborators as the initial step; next, establishing a fluid, thermal, and chemical coupled multi-physics finite element model under the exact experimental conditions and using properties of the same materials as ones used in the VARIM experiment performed; then, generating temperature history datasets from the validated simulations; and lastly, developing a deep convolutional neural network (CNN) and recurrent neural network (RNN)/long short-term memory (LSTM)-based ML model to predict the full field threedimensional temperature distribution as a function of time during the VARIM process. Taking advantage of its accurate and fast prediction capabilities, the developed ML framework is extended to establish the link between the spatio-temporal temperature mapping and key processing parameters. The fast predictions from this ML-based model with a period of a few seconds enables operators to monitor and adjust the manufacturing conditions in real time so that the part temperature can be maintained in a certain range to avoid defects from occurring. Promising prediction results of the model developed in this study demonstrate the potential of the model for process optimization and control by tuning the parameters

The rest of the paper is organized as follows. A physics-based finite element model is introduced first for the simulation of the VARIM process. Next, the physics-based simulation model is validated by a VARIM experiment. In "A deep neural network-based machine learning (ML) model for the VARIM process" section, the machine learning model with a general deep learning structure is developed, consisting of a CNN-based autoencoder for spatial feature extraction, and an RNN/LSTM-based temporal model for predicting the temperature evolution during the VARIM process. This CNN-RNN/LSTM model is trained using the finite element simulation results that are validated by a VARIM



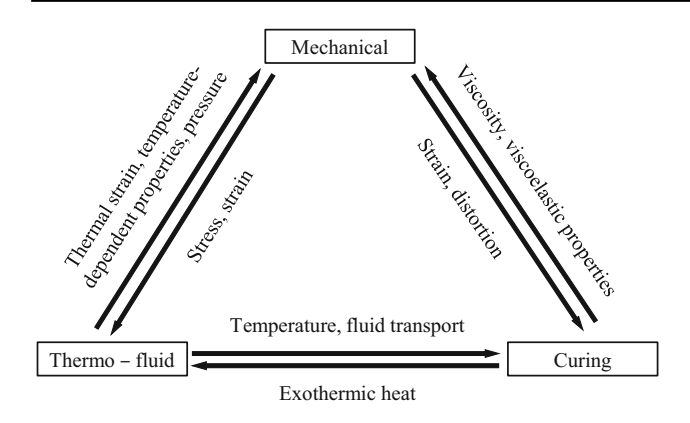


Fig. 1 Multi-physics coupling mechanisms in the composite curing process

experiment on a composite laminate plate of 2 m by 0.56 m by 6.8 cm, with a length-to-width ratio of about 4:1. The model is tested to be capable of predicting the full-field temperature history, and further extended to predict the full-field temperature distribution at the end of the resin curing process based on key processing parameters, including four external control temperatures, which are designated critical in causing uneven epoxy resin curing process and further inducing thermal buckling and other defects in the fully cured glass fiber epoxy composite parts, if not carefully optimized and controlled. Finally, remarks are made on the expansion of the proposed framework to real-time process control and application to wind turbine blade manufacturing.

A physics-based model for VARIM and composite curing processes

We describe first the framework for the multi-physics simulation framework for the resin curing process. Composite curing involves the coupling of curing kinetics, thermofluids, and thermo-mechanical simulations as shown in Fig. 1. The mathematical model for each physical process is described in Table 1. The commercial code PAM-RTM and ABAQUS have been employed for simulations of the VARIM and curing processes. For this work, we focus on the coupling between thermo-fluidic behavior and curing kinetics. The governing equations are briefly described below.

In an infusion-based curing process, the flow of polymer medium such as epoxy resin in the fiber fabric follows Darcy's law, given as

$$\begin{bmatrix} v_x \\ v_y \\ v_z \end{bmatrix} = -\frac{1}{\mu} [K] \begin{bmatrix} \frac{\partial p}{\partial x} \\ \frac{\partial p}{\partial y} \\ \frac{\partial p}{\partial z} \end{bmatrix}, \tag{1}$$



in which v_x , v_y and v_z are the flow velocity in the x, y, and z-direction, μ is viscosity assuming Newtonian flow, p is pressure, and the matrix [K] is known as the permeability tensor and has nine components in general.

The thermal/chemical equation is

$$\rho C_p \frac{\partial T}{\partial t} + \rho_r C_{pr} v \cdot \nabla T = \nabla \cdot (\kappa \cdot \nabla T) - \rho_r \Delta h \frac{d\alpha}{dt}, \quad (2)$$

in which ρ and ρ_r are the mass densities of the composite and epoxy resin, respectively; C_p and C_{pr} are the specific heat of the composite and epoxy resin, respectively; T is temperature, v is the flow velocity resolved from Eq. (1). The second term represents the convection effects and ∇ is the gradient operator, the third term is the diffusion term with κ the conductance matrix, and the last term is due to the chemical reaction in which Δh is the enthalpy of resin polymerization and α is the curing degree resolved from the kinetic model as described next.

The kinetic equation is given as

$$\dot{\alpha} = f(T, \alpha), \tag{3}$$

in which α is the degree of curing and f is a function of temperature and curing degree in the kinetic model. In this study, we use an isoconversion curing kinetic model, which is derived based on the well-known Kamal-Sourour model (Kamal & Ryan, 1980; Kamal & Sourour, 1973).

The isoconversion curing kinetics model is given as

$$\beta \frac{d\alpha}{dT} = A(\alpha) \exp\left(-\frac{E(\alpha)}{RT}\right) f(\alpha), \tag{4}$$

in which β represents the heating rate, E is the activation energy, A is the pre-exponential factor.

Taking logarithmic on both sides of Eq. (4) gives

$$\ln \frac{d\alpha}{dt} = \ln(A(\alpha)) - \frac{E(\alpha)}{RT(t)} + \ln(f(\alpha)). \tag{5}$$

From the above isoconversion curing kinetics model, the curing degree is expressed as

$$\frac{d\alpha}{dt} = A(\alpha) \cdot f(\alpha) \cdot e^{-\frac{E(\alpha)}{RT(t)}}.$$
 (6)

Once the parameters are identified by fitting the modeling results to the experimental data, the curing degree is calculated from the given temperature history recorded from experiments, which is shown in Fig. 2.

Heat convection is described by Newton's law of cooling,

$$\dot{Q} = hA\Delta T(t),\tag{7}$$

Table 1 Key physics and mathematical models for the simulation of the VARIM process

Physics	Phenomenon	Mathematical model	Code
Rheology	Flow in porous media	Darcy's law	PAM-RTM
	Variation of viscosity	Constitutive law (Newtonian or non-Newtonian)	
Thermal	Mold: conduction, and loss from the surface	Heat equation, transfer coefficient (convection)	
	Part: heat conduction, convection, and generation; superficial heat loss	Equation of convection–diffusion with source term	
Chemical	Transport of chemical species, diffusion, polymerization	Equation of convection–diffusion with source term, and kinetic model (Kamal-Sourour)	
Mechanics*	Distortion/buckling, curing-induced residual stress, shrinkage of resin/composite in cure	Conservation of linear momentum (Newton's 2nd law), micromechanical model, and thermal expansion model	ABAQUS

^{*}The multi-physics processes and models are not considered in the scope of this study

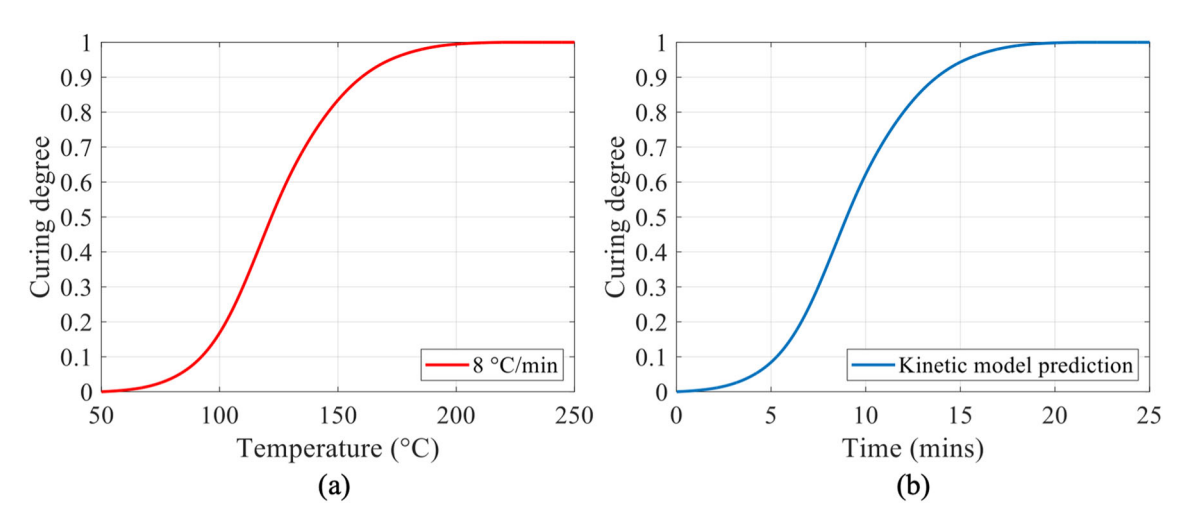


Fig. 2 The curing degree as a function of temperature and time, as calculated from the measured temperature history in an experiment: a Curing degree as a function of temperature; b Curing degree as a function of time

where \dot{Q} is heat transfer rate, h is the convective heat transfer coefficient, A is heat transfer surface area, and $\Delta T(t)$ is the temperature difference between the environment and the composite laminate made in the VARIM, which is the time-dependent value.

To solve the coupling equations describing different physical processes, the resin flow and thermal/chemical equations are resolved first. Detailed simulation steps and model calibration/validation processes are provided in the following sections.

Physics-based model calibration and validation by a VARIM experiment

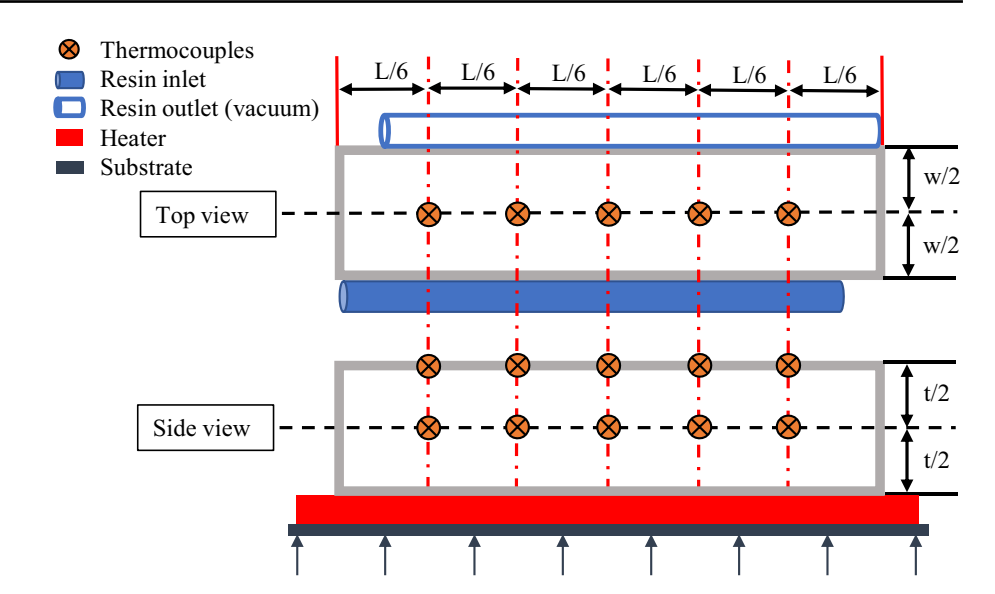
Optimization of the entire composite manufacturing process requires the collective efforts of experiments, high-fidelity simulations, and a fast-prediction digital twin for monitoring and analyzing the actual manufacturing progress in real-time. In the first step, the physics-based model is calibrated and validated by the experiment.

A VARIM experiment conducted in the factory

Figure 3 shows the top and side views of a small-scale VARIM experiment set up for a composite plate of dimensions of 6.8 cm by 2 m by 0.56 m. The glass fibers used are UD1800 (SAERTEX GmbH & Co.KG, Germany), and



Fig. 3 Schematic of the designed VARIM experiment setup



the epoxy used is 780E/786H-B (OlinTM EPOXY, USA). The epoxy resin inlet and outlet are located on the opposite side of the 44-ply glass fiber sheet pileup, which is stacked on top of the heating table. A total of ten thermocouples are placed at the mid and top layers to continuously record the temperature. The number and the locations of the thermocouples are determined based on past experiments, and information from the reference (Ma et al., 2017), where a similar setup was practiced so that the VARIM experiment and the modeling accuracy are not affected.

A 3D view of the actual experimental setup is shown in Fig. 4 with the inset illustrating the part layup. The lab-scale VARIM experiment was conducted at TPI Composites, Inc. Three primary steps include: laying up and flattening each ply of the 44-layer unidirectional dry glass fabric with the flow media, Teflon peel ply, and bagging film inserted at different locations between the glass fabric plies as illustrated by the inset in Fig. 4; pre-fixing epoxy resin with resin hardener; and arranging the resin feed line at the inlet and vacuum outlet. Six batches of mixed epoxy resin weighing 28.4 kg are used to infuse 44 plies of glass fabric (UD1800: unidirectional, 1800 g/m²) with a total mass of 85.5 kg. The entire VARIM process is performed in a composite cleanroom on a table made of the same glass fiber epoxy composite with heating elements attached so that the heat applied from the bottom is precisely controlled. The epoxy resin feed line and vacuum outlet are located on the opposite side of the glass fiber sheet layout, with a 0.2 m wide buffer zone arranged to ensure a good flow of the liquid-state epoxy resin. Similar to the large wind turbine blade manufacturing process, flow media is also used to enhance the epoxy resin flow at the interface of the glass fiber sheet and the tabletop surface, and multiple studies exist on estimating the heterogenous permeability of this distribution media (Gokce et al., 2005; Yun et al., 2018).

The thermocouples placed at all ten locations and the table surface record the temperature profiles as shown in Fig. 5. It is noted that the resin infusion process ends after 60 min, after which both resin inlets and outlets are closed and sealed to maintain the vacuum inside the vacuum bag. A blanket is used to cover the entire composite top surface to reduce heat loss. The table heating temperature is set to 45 °C during the first 200 min, then increased to 80 °C and kept for another 100 min, and subsequently reduced to 20 °C until the end of the experiment as indicated by the red line in Fig. 5. The heating temperatures, 45 °C, 80 °C, and 20 °C, and their corresponding durations are similar to the ones in the actual blade manufacturing process.

The overall temperature trends at all ten locations are synchronized, and temperatures at the five locations at the mid surface are slightly higher than the ones on the top surface. This is largely due to the following two reasons: First, the heat is transmitted from the heaters on the bottom through mid surfaces to the top layers, during which heat spreads across all layers. Thermal convection between the top layers and the environment leads to more heat loss compared to the mid surface. Second, the surface cover is removed at the time around 370 min, and the tabletop temperature is set back to 20 °C, which causes a steep drop in temperature as observed in all locations. The recorded temperature provides important information and insight regarding the epoxy resin curing progress. The temperature data is also used to calibrate the physics-based simulation model as detailed in the following section.



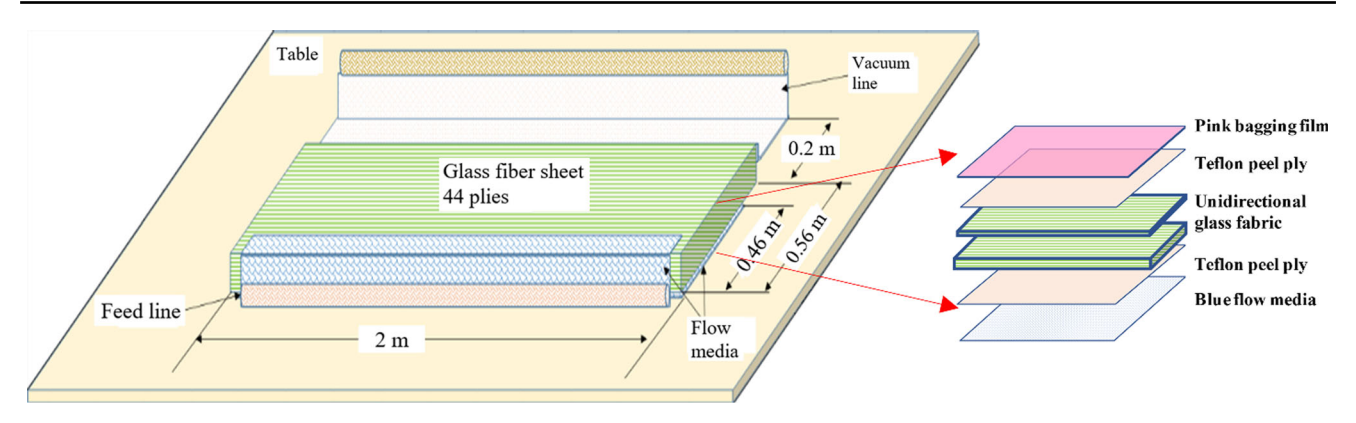
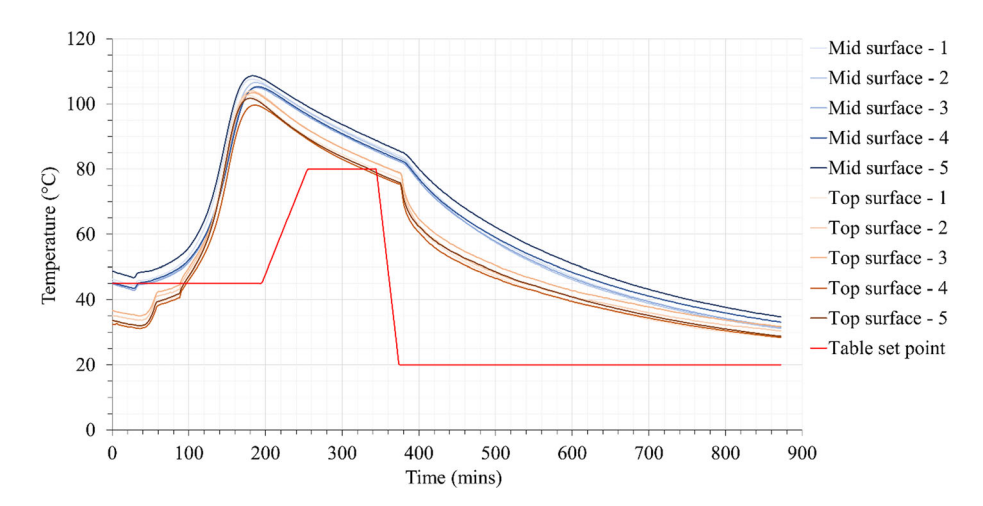


Fig. 4 Schematic diagram, including the part layup inset, of the VARIM experiment conducted in the TPI Composites, Inc. laboratory

Fig. 5 Temperature readings at all ten locations of the VARIM experiment (Color figure online)



Physics-based model calibration and validation using experimental data

Infusion and curing simulations are conducted using the commercial code PAM-RTM, which provides multi-physics based simulation capabilities using models listed in Table 1 and described in "A physics-based model for VARIM and composite curing processes" section. The primary objective of the simulations is to establish a validated model based on the VARIM experimental setup described in "A VARIM experiment conducted in the factory" section.

To calibrate the model, we compare the simulation results with the experimental data, so that the finite element model generates very closely matched resin flow and temperature results. Material properties and parameters for the boundary conditions used in the model are shown in Table 2. The ones calibrated from the experiment are marked by asterisks. Material properties of the epoxy resin used in the experiment, including density, coefficient of thermal conductivity, Newtonian viscosity, and specific heat, are obtained directly from the specs sheet provided by the epoxy resin manufacturer. The principal directions of the permeability tensor of the glass fiber sheet are assumed to align with the in- and

out-of-plane directions of the glass fiber sheet and the corresponding components are given as Kx, Ky, (in-plane), and K_z (out-of-plane). These values are calibrated based on the recorded resin front flow from the experiment. The coefficient of thermal conductivity of the resin-infused preform is taken from the reference (Ma et al., 2017), which is measured on a similar system using the same materials. Two types of boundary conditions are prescribed. The first is the temperature imposed, including the environment air temperature, which is set to be 20 °C, and the tabletop temperature, which is prescribed according to the temperature history given in Fig. 5. The second is the convection coefficients, including the ones between the tabletop and the composite, and between the composite top and the environment air. According to the baseline values measured and principles explained in the reference (Ma et al., 2017; Struzziero & Teuwen, 2019), the convection coefficient between the tabletop and the composite is set at 5.5 W/($m^2 \cdot K$), since the contact media has not changed during the experiment. The convection coefficient between the composite top and the environment is calibrated to match the temperature readings of the thermocouples from the experiment. Thermal insulation is applied 60 min into the



Table 2 Material properties and imposed boundary conditions in simulations

Material properties	Epoxy resin (780E/786H-B, Olin™ EPOXY)	Coefficient of thermal conductivity $[W/(m\cdot K)]$ Density (kg/m^3)		0.35
				1083
		Newtonian viscosity (N· s/m²)		0.8
		Specific heat [kJ/(kg ·K	[()]	2.5
		Enthalpy (kJ/kg)		450
	Glass fiber sheet (UD1800, SAERTEX GmbH & Co.KG)	*Permeability (m ²)	K_x	8×10^{-10}
			K_y	2×10^{-10}
			K_z	8×10^{-12}
	Resin-infused preform	Coefficient of thermal conductivity $[W/(m \cdot K)]$		0.6
Boundary conditions	Temperature imposed (°C)	Air		20
		Tabletop set point		See Fig. 5
	Convection coefficient [W/(m ² · K)]	*Tabletop & composite		5.5
		*Composite top & environment		See Fig. 8b

^{*}Properties are calibrated in simulations to match experimental results

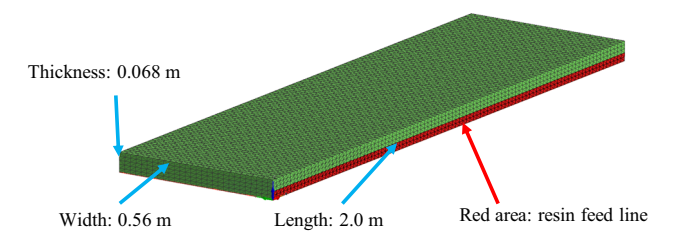


Fig. 6 A computational model for the composite laminate plate of 2 m \times 0.56 m \times 0.068 m. A total of 84,000 tetrahedron elements with an element side length of 1.28 cm are used

experiment and removed at around 370 min to capture the effects of the blanket.

The computational model is shown in Fig. 6. A total number of 84,000 tetrahedron elements with an edge length of 1.28 cm are used. To calibrate the heterogeneous permeability values, the simulated epoxy resin front flow is compared with the recorded results of the VARIM experiment as shown in Fig. 7. The most important variables contributing to the kinetics results include the permeabilities of the flow media, and permeabilities K_v and K_z in the transverse cross-section directions as denoted in Fig. 7c. As the flow media enhances the epoxy resin flow, the epoxy resin fills the bottom of the composite first as observed in the VARIM experiment, which is also simulated in the model as illustrated by the crosssectional view of the 3D resin infusion simulation in Fig. 7c. By iteratively changing the permeability values in the x, y, and z directions to match the epoxy resin front position at different time steps as recorded by images from the VARIM experiment, such as Fig. 7b, a good fit of the simulation and experimental results is achieved as shown in Fig. 7a. Calibrated permeability values K_x , K_y , and K_z are listed in Table 2.

As the epoxy resin front flows and the curing processes are coupled in the finite element model, the temperature results from the simulations need to be calibrated to match the experimental results. This is done by adjusting the thermal convection coefficient values between the tabletop and the composite, and between the composite top and the environment. The initial thermal convection values are set based on data from the published literature (Ma et al., 2017), where the same composite and epoxy resin materials were used. Other material properties of the epoxy resin, including density, coefficient of thermal conductivity, Newtonian viscosity, and specific heat, are obtained directly from the specs sheet provided by the epoxy resin manufacturer. This ensures that the material properties in the model are set correctly. In the simulation, the same tabletop set point heating history, as shown in Fig. 8a and applied in the VARIM experiment, is used in the model. The heating history is identified by two stages since the thermal insulator cover is removed at about 370 min. After multiple iterations, temperature histories of the mid and top surfaces of the composite from the simulation match the VARIM experimental results as shown in Fig. 8c, with the convection coefficient value between the composite top surface and the environment air calibrated as shown in Fig. 8b. Figure 8d–g present visualizations of the spatial temperature distribution from the calibrated simulations at four different time steps during the resin curing process.

All the physics-based simulations are performed using parallel computing executed on a workstation with an Intel i9-10900X CPU (10 core with 3.7 GHz base frequency) and 32 GB memory. The total computational time for the model



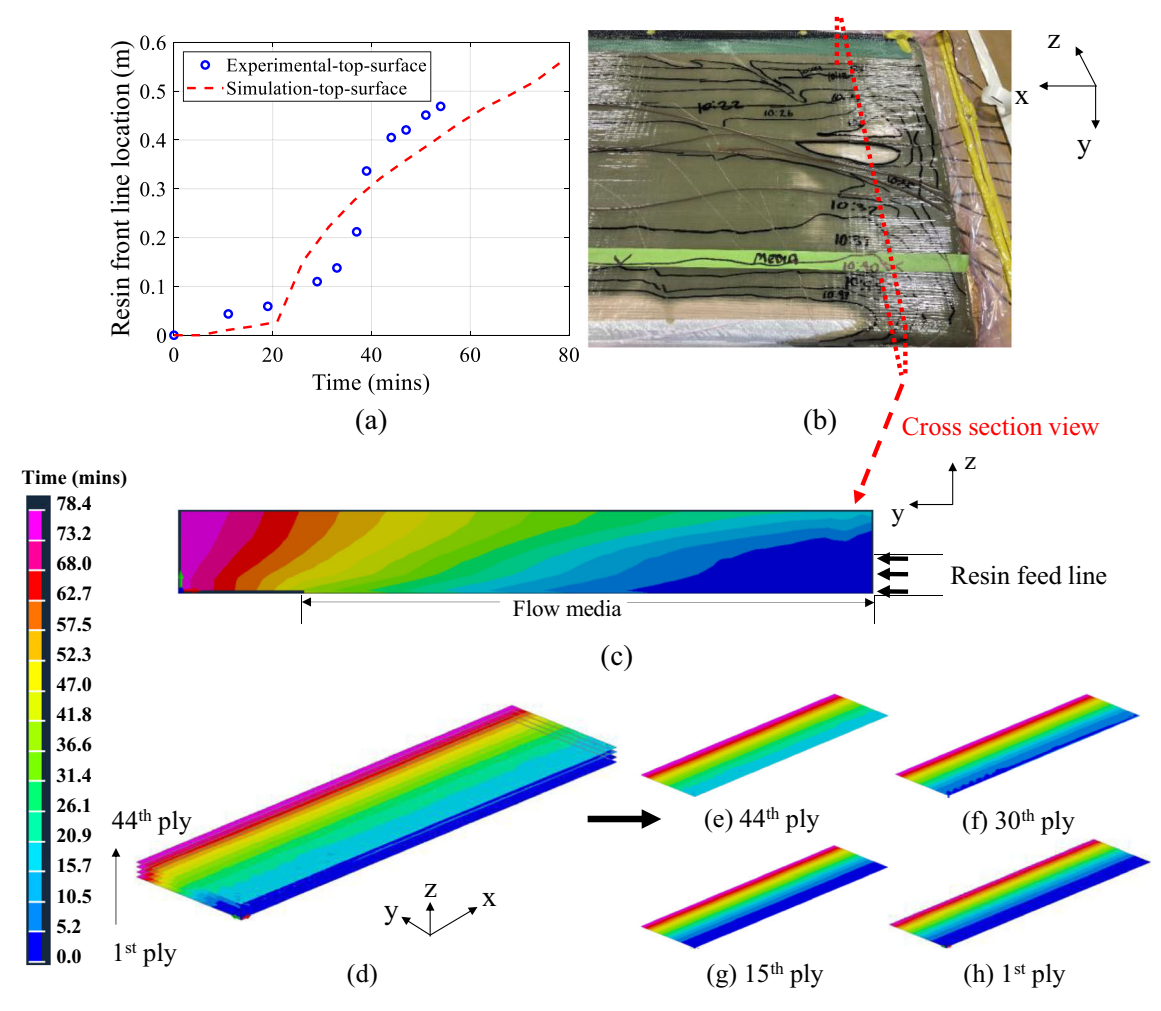


Fig. 7 Calibration process of heterogeneous permeabilities of the glass fiber composite: **a** Comparison of resin front flow on top surface from experiment and simulations; **b** Image of VARIM experiment showing cross sections used in calibrations as marked in red; **c** 2D transverse

y–z cross-section of finite element infusion simulations; ${\bf d}$ 3D visualizations of the epoxy resin infusion simulations; ${\bf e}$ – ${\bf h}$ Infusion results on different plies of the composite (Color figure online)

is 574 s, including 218 s for the 3D resin infusion process, and 356 s for the separate resin curing process.

A deep neural network-based machine learning (ML) model for the VARIM process

Transfer the non-image data to images and data preprocessing

To fully utilize spatial and temporal information from the physics-based model as described in "Physics-based model calibration and validation by a VARIM experiment" section, all nodal temperatures obtained from the finite element analysis are converted into the image format. This is a common practice for many applications where multiple methodologies have been developed to transfer non-image data, such as

tabular data, into images for deep learning with convolutional neural networks (Sharma et al., 2019; Zhu et al., 2021).

The complete process of transferring the nodal information to images is illustrated in Fig. 9. The mesh used in 3D simulations is shown in Fig. 9a. Figure 9b and c show the nodal distribution on each plane. Next, model data containing the spatial coordinates and temperature value of each node are merged in tabular form. A total of 102, 30, and 6 distinct x, y, and z coordinate values of all nodes are identified and converted to the closest integer values as required by CNN. Since the 6 z values provide the position of 6 layers, the conversion leads to an array of size 30×102 filled with temperature values for each of the six layers. One row and one column are void after the transformation due to the lack of computational nodes at these locations. The void space is "patched" with the average of the neighboring values, and images containing the temperature information at different



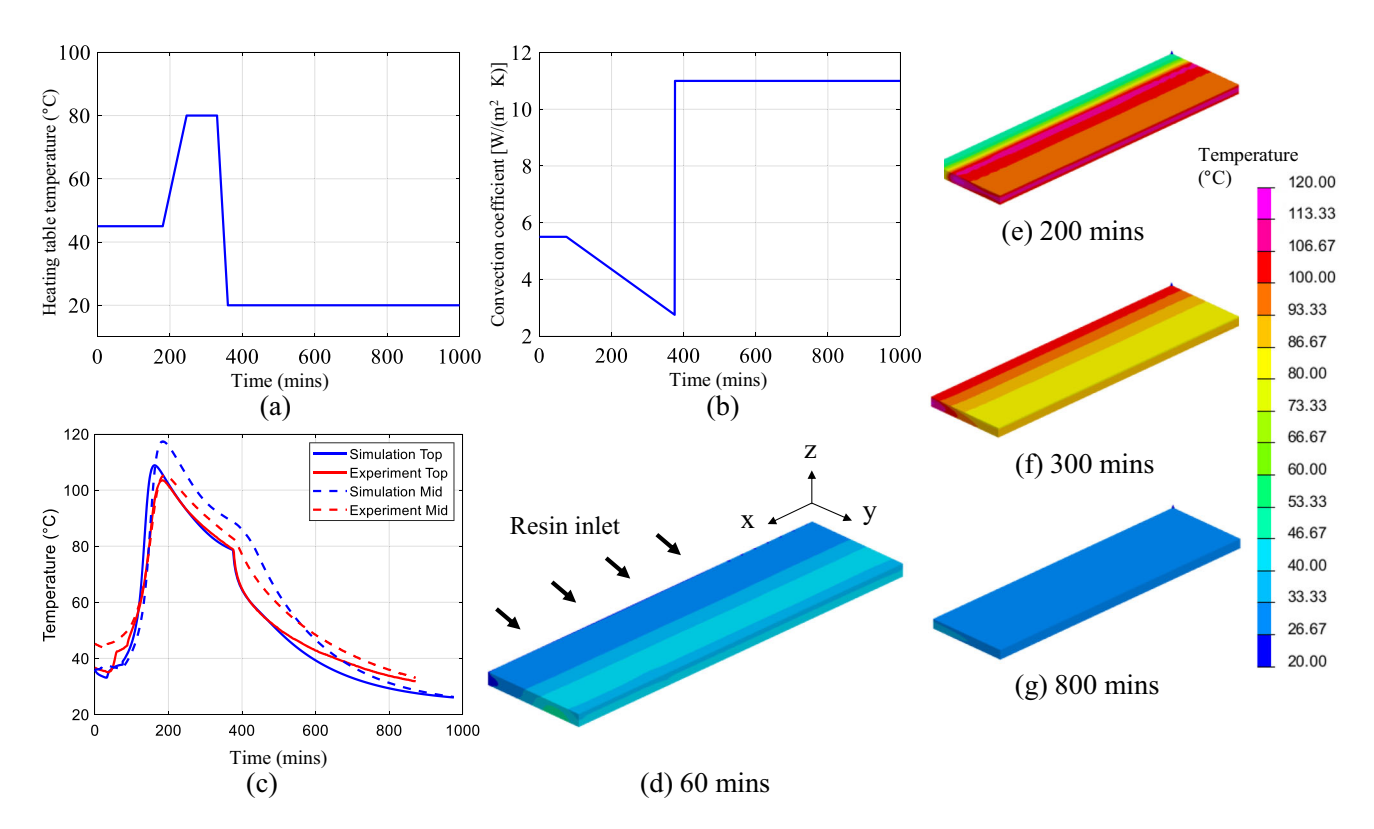


Fig. 8 Calibration process of the simulation model to match the temperature distribution from experiments during the epoxy curing: **a** The tabletop set point heating history of the VARIM experiment; **b** The convection coefficient between the composite top surface and the environment air in the simulation model used in the calibrated simulation;

 ${\bf c}$ The temperature history of the mid and top surfaces of the composite from the simulation and the VARIM experiment results; ${\bf d}$ – ${\bf g}$ The temperature distribution from simulations during the epoxy resin curing process at 60, 200, 300, and 800 min, respectively

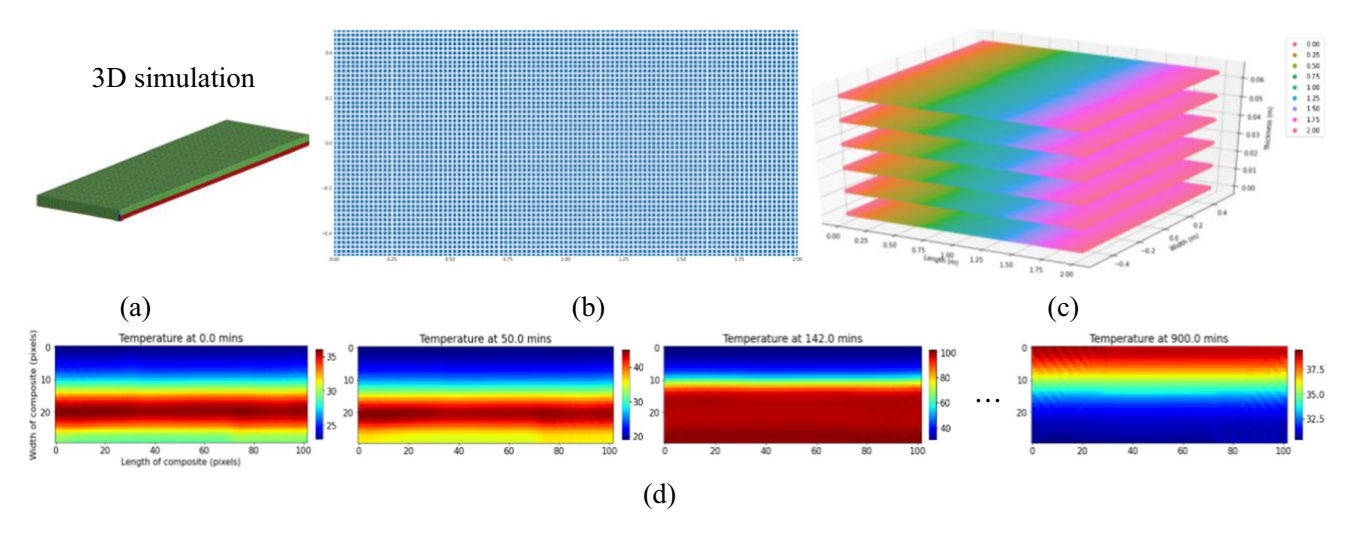


Fig. 9 An illustration of transferring data from the physics-based model to images **a** 3D simulation in PAM-RTM; **b** Distribution of nodes on the 2D plane; **c** Visualization of all six planes in the 3D space; **d** Images obtained from nodal information after data processing



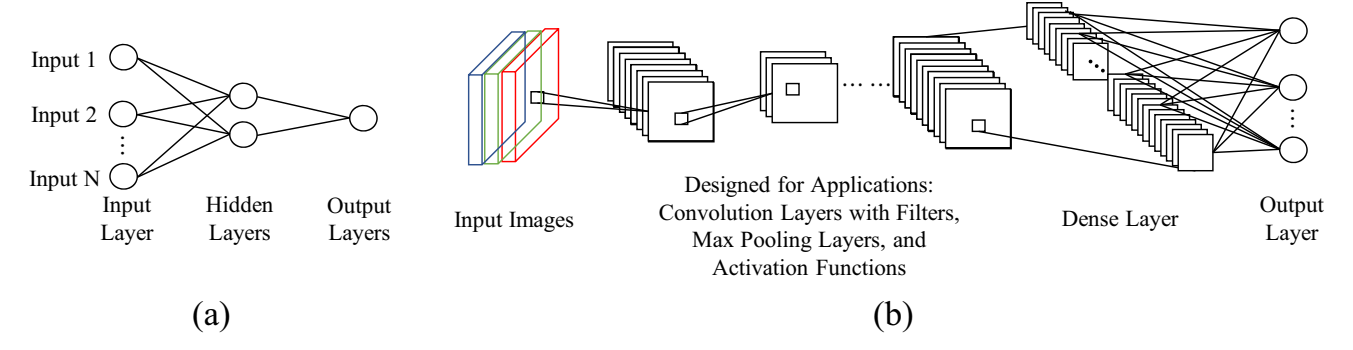


Fig. 10 The basic structure of (a) an artificial neural network (ANN), and (b) a convolutional neural network (CNN) with three-channel images as inputs

time steps are obtained as shown in Fig. 9d. All data preprocessing is done using Jupyter Notebook in Python 3.9 environment.

A spatio-temporal temperature predictor based on a deep CNN-RNN/LSTM model

CNN is one type of ANN, which are computational processing system inspired by the working principles of biological neuron systems. The basic structure of an ANN is shown in Fig. 10a, where the input data in the format of a multidimensional vector is delivered to each artificial neuron, and then produces a single output that is sent to multiple other neurons (Jain et al., 1996; Krogh, 2008). The output from each neuron is the weighted sum of all the inputs plus a bias term, which is then output after being processed by the activation function. The neurons are typically organized into multiple layers, noted as hidden layers. A complete neural network stacked up with many hidden layers sequentially is known as deep learning (Goodfellow et al., 2016), which is found to be much more effective in improving the mapping from inputs to outputs by adjusting parameters in each neuron (Lecun et al., 2015). CNN is commonly used to extract image-specific features by applying many convolution kernels or filters that slide along the inputs (Albawi et al., 2018). After comparing the output after each forward propagation with the expected ground truth values using the loss function, the total error with respect to parameters in each layer is calculated and back-propagated from the output layer to the first hidden layer (Rumelhart et al., 1986). Through many such iterations, all parameters of the entire neural network are optimized to best project the output based on the inputs. A representation of a CNN architecture with multi-channel images as inputs, repetitive convolutional layers with filters, pooling layers, and activation functions, the dense layers, and the output layer is shown in Fig. 10b.

During the curing process, the temperature profiles are sets of 4D data, consisting of the temperature at each point

in the composite system at different time steps. Therefore, to account for both spatial and temporal developments of the temperature information, specific types of the neural network, the recurrent neural network (RNN), as well as the derived and modified version of it, i.e., the network with long short-term memory (LSTM) units are employed. Their structural units are illustrated in Fig. 11.

RNN is one kind of ANN, which takes in an entire sequence of data at different time steps t as inputs x_t into each unit. With the repetitive units connected sequentially as shown in Fig. 11a, this structure can make predictions along the time domain based on the trained network and the previous inputs (Abiodun et al., 2018). However, this structure is known to often fail to "remember" the long-term information in the time series data due to vanishing gradient problems during the backpropagation training process (Hochreiter, 2011; Lipton et al., 2015). So the unit cell of the RNN has been modified and improved into the LSTM unit as one example is shown in Fig. 11b (Olah, 2015). LSTM can "remember" the long-term information using three different gates, i.e., the forget gate (f_t) , the input gate (i_t) , and the output gate (o_t) , each of which process is expressed by Eqs. (8), (9), and (10), respectively, to control the weight of historical information and new information input from the current state (Hochreiter & Schmidhuber, 1997; Gers et al., 2000, 2002). The cell state (C_{t-1}) is passed through the entire network with small interactions with each unit. The forget gate decides the amount of information from the cell state to be discarded, and the input gate determines what new information is going to be stored in the cell state, which is added to the created vector \tilde{C} . tthat contains new candidate values (Olah, 2015). Finally, the output gate will filter out parts of the cell state by running the sigmoid function first, and then put the cell state through the tanh function by multiplication, so that the entire unit only outputs the parts that are desired. The details of each step are shown in Eqs. (8)–(12).

$$f_t = sigmoid(W_f \cdot [h_{t-1}, x_t] + b_f), \tag{8}$$



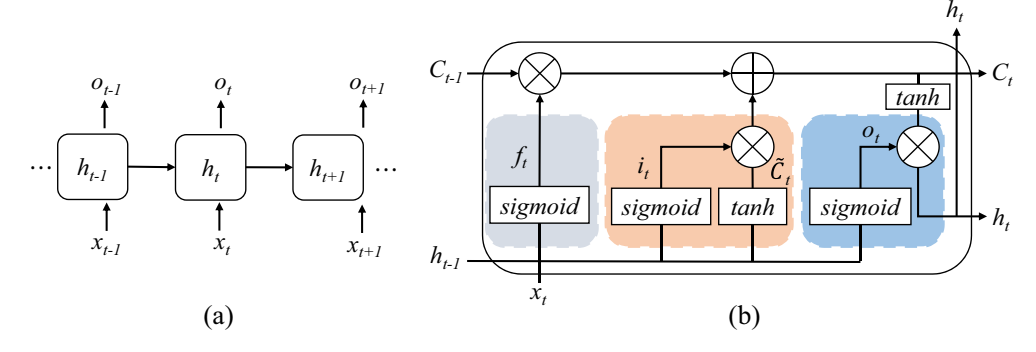
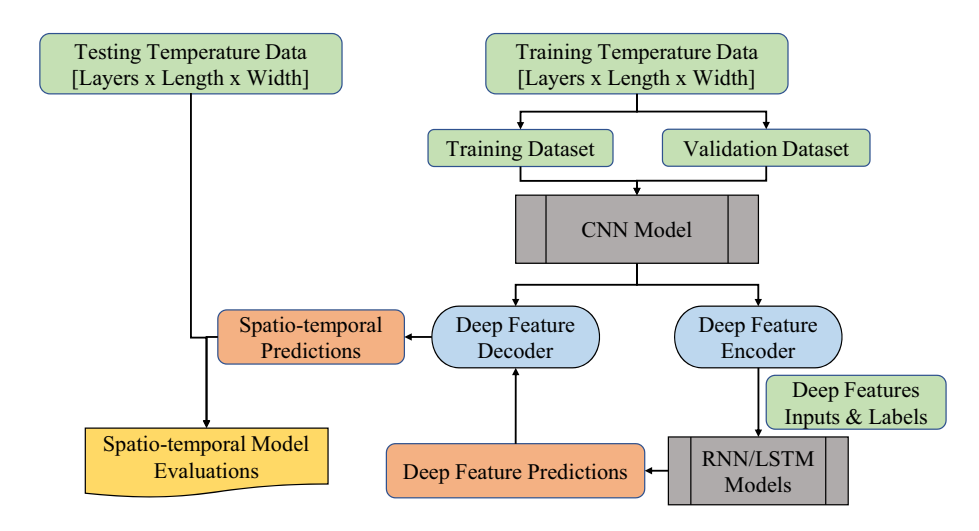


Fig. 11 The basic structure of (a) a unit of a recurrent neural network (RNN), and (b) an example of a long short-term memory (LSTM) unit (Olah, 2015)

Fig. 12 Framework of training and testing the CNN-RNN/LSTM-based spatio-temporal model



$$i_t = sigmoid(W_i \cdot [h_{t-1}, x_t] + b_i), \tag{9}$$

$$o_t = \tanh(W_C \cdot [h_{t-1}, x_t] + b_o), \tag{10}$$

$$C_t = f_t \cdot C_{t-1} + i_t \cdot \tilde{C}_t, \tag{11}$$

$$h_t = o_t \cdot tanh(C_t). \tag{12}$$

Utilizing the spatial features extraction functionality of CNN and the sequential data processing capability of RNN/LSTM structures, a spatio-temporal framework for temperature predictions is established and presented in Fig. 12. This spatio-temporal model is based on an integrated ML model coupled with the design of the deep neural network. Specifically, a CNN-based feature autoencoder is used to extract and translate the spatial deep features from the input images (Hinton et al., 2006; Rumelhart et al., 1985), and an RNN/LSTM-based structure is employed as a temporal predictor to forecast such deep features along the timeline, given the temperature mapping at the past time steps. Such autoencoder designs are widely used in many applications (Hinton et al., 2011; Kingma & Welling, 2019), including computer

vision (Pathak et al., 2016; VincentPascal et al., 2010), natural language processing (Devlin et al., 2018; He et al., 2022), porosity extraction in wire-arc additively manufactured aluminum (Zhang et al., 2023), wind speed prediction (Chen et al., 2021), and many more.

The input to this spatio-temporal model is the temperature mapping at all time steps obtained from the experimentally validated simulation results in the image form of 30 × 102 arrays with values normalized and preprocessed as described in "Transfer the non-image data to images and data preprocessing" section. Figure 13 shows the details of this CNN—RNN/LSTM—CNN architecture. In the construction of the ML model, different architectures, specifically, combinations of different numbers of convolutional layers, filter size, stride number, activation functions, UpSampling size, number of hidden units, etc., for the CNN-based autoencoder and RNN/LSTM-based temporal models are considered, which have a great impact on the model performance. After many attempts, the structures shown in Figs. 13 and 14b, are determined due to their higher prediction accuracies than others. The input images first go through the CNN-based encoder part such that the deep features embedded with the spatial information of the temperature distribution among the



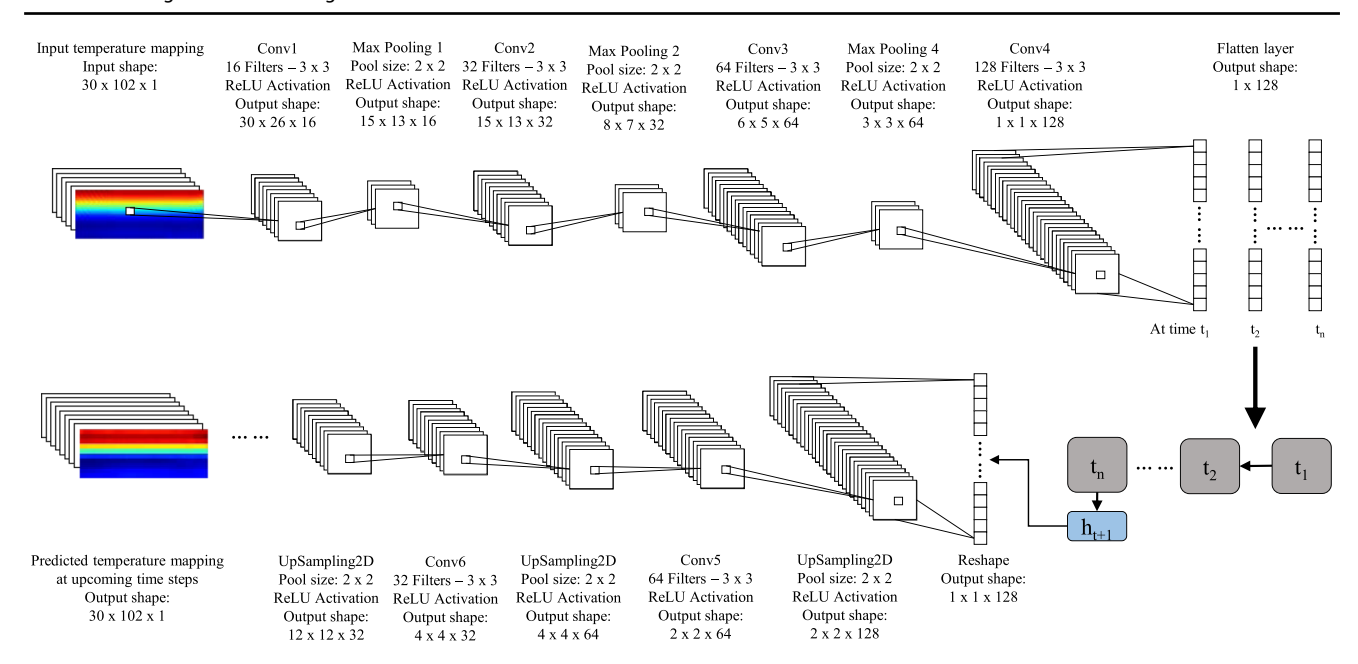


Fig. 13 Flowchart of the CNN (encoder)—RNN/LSTM—CNN (decoder) architecture for spatio-temporal curing temperature predictions

entire composite system are extracted and encoded into a 1D array with a size of 128 (number of extracted features) after the flatten layer. Next, the RNN/LSTM-based temporal predictor takes in a number of those time-series deep features to forecast the resulting sequences in the time domain as the output. Then, the predicted deep features are fed to the CNN-based decoder part to reveal the projected temperature mapping. The time step in this study is chosen to be 5 with a step size of 100 s, which means that the curing temperature records of the last 500 s are collected to predict the temperature profiles in the subsequent 100 s.

A CNN-based model to link processing parameters to the temperature mapping

In the second ML model, the aim is to predict the effects of the VARIM processing parameters, so that the process can be optimized to minimize the defects induced by uneven temperature distribution in different regions. It is known that temperature history during the VARIM process, including the epoxy resin curing, is the primary factor determining the composite part quality. A typical temperature history of VARIM is illustrated in Fig. 14a. Four temperatures, T₁ holding temperature during the initial heating stage, T₂ the end temperature of the heating ramp, T₃ the starting temperature of the heating decline, and T₄ the last holding temperature, are designated as the key parameters and inputs to the model. In addition, to account for the temperature variation

in the spatial domain, the layer number of composite planes is included as the fifth input parameter in the model. The complete model is established to predict the temperature distribution in the composite part at 400 min after the VARIM process is started, which is considered as the finishing time of the primary epoxy resin curing process, based on the material properties and experimental characterizations of the curing of the epoxy resin used in this study.

The proposed ML framework is shown in Fig. 14b and is inspired by many established and well-known CNN designs, such as AlexNet, VGG-16, ResNet, etc. (He et al., 2015; Krizhevsky et al., 2017; Simonyan & Zisserman, 2014), that can accurately map the image inputs to different categories. In this study, a regression model is established herein, where the values of the five processing parameters, including T_1 (the initial heating temperature), T₂ (the end temperature of the heating ramp), T₃ (the starting temperature of the heating decline), T₄ (the last holding temperature), and the spatial temperature mapping are all considered continuous rather than discrete. During the model training process, the same regression metrics, MeanAbsolutePercentageError (MAPE), or "mape" function in the TensorFlow Keras library is used. The design of this model is to reflect the optimization need in the manufacturing process, during which externally applied temperatures affect the quality of the composite part. All five parameters can be optimized to produce high-quality glass fiber composite parts.



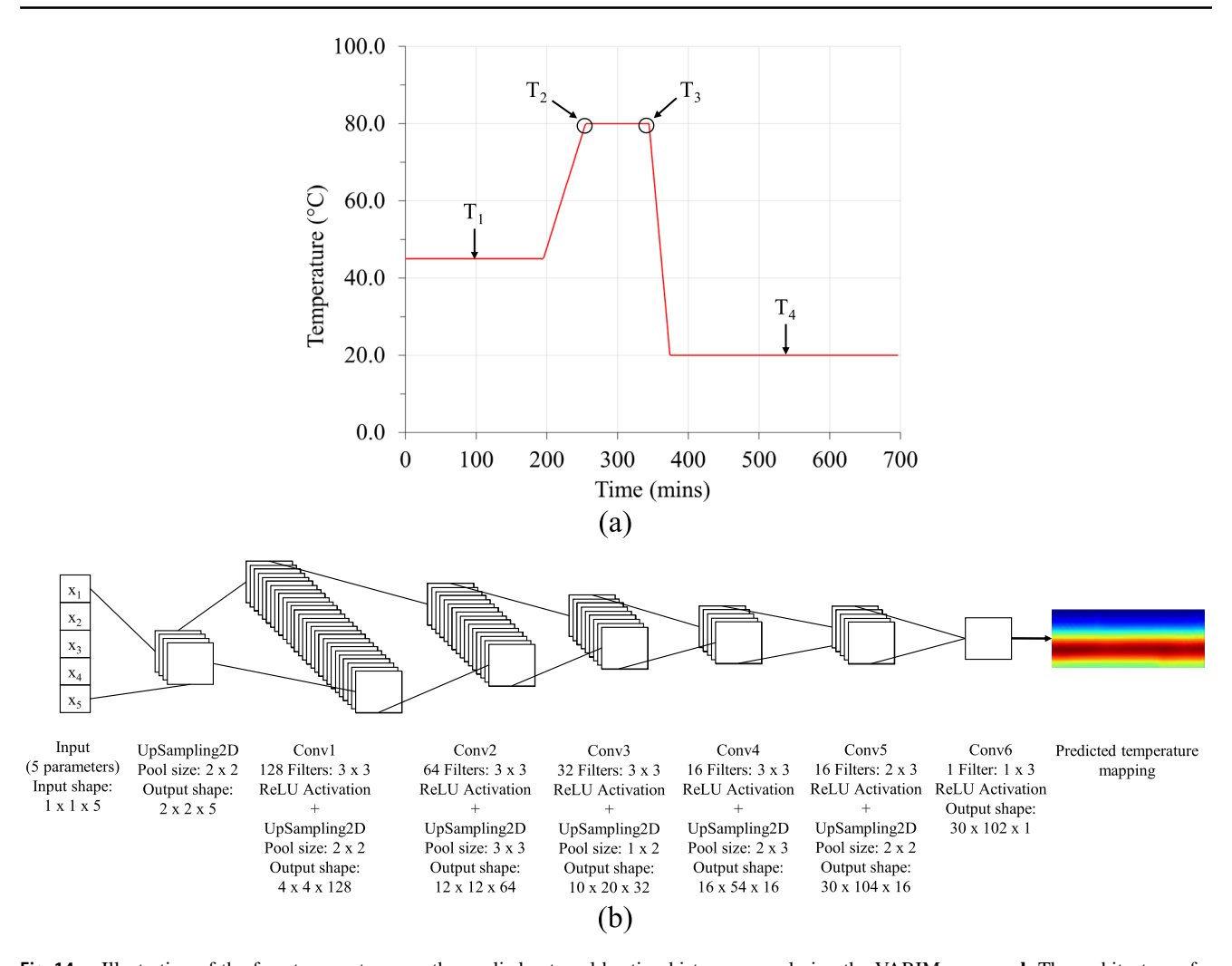


Fig. 14 a Illustration of the four temperatures on the applied external heating history curve during the VARIM process; **b** The architecture of a CNN-based deep neural network to predict the temperature mapping at 400 min from five input processing parameters

Results and discussions

The experimentally validated simulation results are used to train and validate all the ML models. Two types of datasets are generated and converted into image formats, including the time-series 3D temperature distribution for the spatio-temporal predictor, and the dataset of the processing parameters to single temperature mapping. The datasets used by different machine learning models are listed in Table 3. All datasets are divided into two groups at a ratio of 4:1: one group for training and the other for testing. The training dataset is further separated for training and validation purposes with the same split ratio of 4:1 as a common practice to avoid biased results. This data partition is made automatically using the "train_test_split" function in the "scikit-learn" library to ensure that all data subsets for training, validation, and testing are obtained randomly to avoid bias from selecting the data manually. The entire spatio-temporal dataset composed of a total of 3,246 images, categorized as "Type 1"

in Table 3, is first used to train and test the CNN-based autoencoder. Then 541 images from layer 6 of the spatio-temporal dataset, with each image corresponding to the temperature distribution of the top layer of the composite at every 100 s during the entire VARIM process, are used to train and test the RNN and LSTM models. For the case of the CNN-based predictor of the single temperature mapping from the processing parameters, the "Type 2" dataset of size 3,750 is used for training and testing. Specifically, each of the four temperatures that are designated as the critical processing parameters, T₁, T₂, T₃, and T₄, with the physics meaning illustrated in Fig. 14a, is assigned a temperature value from four different groups, "41, 43, 44, 45, and 46 °C", "79, 80, 81, 82, and 83 °C", "79, 80, 81, 82, and 83 °C", and "20, 21, 22, 23, and 25 °C", correspondingly. It is worth noting that all temperature values are selected based on practices on the manufacturing floor and the most related existing reference (Ma et al., 2017), and this study aims at establishing such an



Table 3 Dataset usage of all machine learning models established in this study

Datasets			Machine learning models			
		Number of images (size: 3246 \times 30 \times 102)	Spatio-temporal predictor		Processing parameters-to-temperature mapping	
Type 1	Layer		CNN-based autoencoder	RNN/LSTM temporal model	CNN-based predictor	
	1 (base)	541	✓	×	×	
	2	541	✓	×	X	
	3	541	✓	×	×	
	4	541	✓	×	X	
	5	541	✓	×	X	
	6 (top)	541	✓	✓	×	
Type 2	$3750 \times \{\text{inputs } (1 \times 5) \text{ \& output images } (30 \times 102)\}$		×	×	/	

ML-based modeling method, instead of seeking their optimal values.

The evaluation metric used is the mean absolute percentage error (MAPE), defined as,

MAPE =
$$\frac{1}{n} \sum_{i=1}^{n} \left| \frac{A_i - P_i}{A_i} \right| \times 100\%,$$
 (13)

where n is the total number of ML model training iterations (epochs), A_i and P_i are the actual and predicted values, respectively, at a different iteration i. The training process of all models is carried out using the TensorFlow software library for machine learning (Abadi et al., 2016), in Python 3.9 environment on a workstation with an Intel i9-10900X CPU, and Nvidia GTX 1080Ti graphic card with GPU training enabled. The training time for all four models, CNN-based autoencoder, RNN-based and LSTM-based temporal models, and the CNN-based parameters-to-temperature model, are 2 min 19 s, 1 min 44 s, 5 min 23 s, and 4 min 30 s, respectively. Once trained, all four models are capable of making predictions within 5.4 s when a total of 3,216 images of all six layers are input to the trained RNN/LSTM models, and a single time frame temperature prediction can be obtained instantly within 100 ms. The primary machine learning model parameters are listed in Table 4, including dataset size, hyperparameters for training ML models, and model testing results. All ML models use the "Adam" algorithm as the optimizer, which is a first-order gradientbased optimization of stochastic objective functions (Kingma & Ba, 2014). The regression metrics MAPE, as shown in Eq. (13), or the corresponding "mape" function from the Tensorflow Keras library, is used to monitor and measure the performance of all models during training and testing. Other hyperparameters, including the learning rate and batch size, are determined from iterative experiments.

The training histories of the CNN-based autoencoder, RNN, and LSTM models are shown in Fig. 15. The definition of "loss" in Fig. 15a is abbreviated and referred to as the loss function calculated as the sum of errors made for each example in training and validation datasets during the model training process. The loss value implies how well or poorly a model performs after each iteration of optimization. The progressing lower loss value indicates the errors between the model prediction and the ground truth are reducing significantly, as also indicated by the MAPE vs. training iteration shown in Fig. 15b. Once trained, they are tested on a separate testing dataset. The results show that all four ML models have a testing MAPE of less than 1.5% as indicated in Table 4.

Spatio-temporal temperature prediction results of the CNN-RNN and CNN-LSTM models

The trained CNN-based autoencoder is used to encode deep features from the raw images, and then the deep features become inputs to train the RNN and LSTM temporal models. Although the RNN and LSTM models are trained on images of layer 6 only, both models show excellent prediction accuracy on images of all six layers, as shown in Fig. 16a and b, where prediction accuracies of RNN and LSTM models are plotted as the average MAPE value of each image at every 100 s during the entire 700 min. Figure 16c—h show and compare the prediction accuracy of the RNN and LSTM models on each of the six layers.

The comparison shows that the overall prediction accuracy is over 94% during the entire time period for both models. Further analyzing the model prediction accuracy at different



Testing MAPE (%) 0.4266 0.2268 0.2947 1.4009 Testing loss 0.0029 0.0140 0.0043 0.0023 Model testing results dataset size Testing 9 9 750 dataset size Validation 82 82 009 Training dataset size 340 340 2400 Total epochs 348 903 723 Batch size 12 12 2 Learning rate 0.001 0.001 0.001 Total parameters Model training
 Fable 4
 Machine learning model parameters
 104,369 18,128 7,508 RNN-based temporal model parameters-to-temperature CNN-based autoencoder STM-based temporal CNN-based model Models

time steps, lower prediction results on composite layers 2, 3, and 4 are observed during the first 20 min into the VARIM process for both models, as indicated by the higher MAPE during the early time steps in Fig. 16d, e, and f, corresponding results of layer 2, 3, and 4, respectively. This is likely due to the temperature changes in the middle of the composite having a different trend compared to the temperature changes on the top and bottom layers, on which the temporal ML model is trained. As the VARIM process is started, the cold epoxy resin first enters the dry and pre-warmed glass fiber composite from the bottom layer on the tabletop, as illustrated by the resin feed line and the blue flow media that guides the epoxy resin flow as shown in Fig. 4. While the resin supply is at the ambient temperature, the glass fiber preform is heated up to 45 °C. The resin heats up as it flows into the system from the inlet to the outlet. Therefore, the relatively cold epoxy resin first infuses the area along the flow media within a short time, which covers parts of the top and bottom layers of the composite as illustrated by the schematic in Fig. 4. Hence the temperature in these areas drops faster than the uncovered area, for example, the middle parts of the composite, which is significantly warmer than the already infused top and bottom sections. This course leads to abnormal and unordered temperature changes that make the prediction challenging for both RNN and LSTM models, as they are trained on the temperature history that is primarily dominated by the curing kinetics of the epoxy resin and the heat transfer under the steady state.

The second noticeable high MAPE of the prediction in Fig. 16 occurs on all layers of the composite before 220 min, especially between 50-200 min, when the accuracy is relatively low, with the maximum MAPE value approximately 3.5% to 4.4% at about 100 to 130 min into the VARIM experiment. This dip in prediction accuracy is attributed to the rapid chemical reaction of the epoxy resin during the early curing process, based on the curing kinetics and the associated heat released by the epoxy resin. This temperature increase in the composite system due to the heat release from the chemical reaction of the resin curing is also observed from the thermocouple data shown in Fig. 5 in which the temperature readings at all ten locations in the composite are climbing under the external heating from the tabletop with a constant set temperature of 45 °C until around 200 min. As the overall system enters a steady state with relatively subtle temperature changes, both RNN and LSTM models are more capable of accurately predicting the temperature mapping. The similar performances of the RNN and LSTM models imply that within the time domain of 700 min and a temporal resolution of 100 s in this study, the RNN does not have the obvious "gradient vanishing" issue as typically reported. However, this can be an issue for datasets with a larger time period or higher temporal resolution.



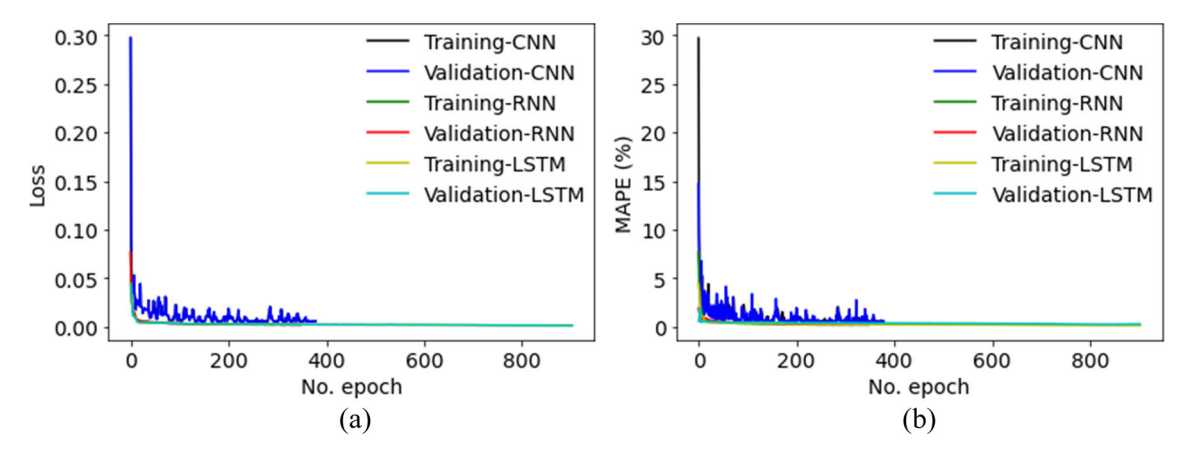


Fig. 15 Training progress of the CNN-based autoencoder, RNN, and LSTM models: a The loss vs. training epoch (iteration); b The mean absolute percentage error (MAPE) vs. epoch

In addition to the assessment of the model prediction accuracy results on temperature as a function of time, it is also necessary to evaluate the predicted temperature mapping at different locations and different time steps from both RNN and LSTM models. To this end, the temperature distribution and evolution on layer 1 are visualized as shown in Fig. 17. The selected time steps are 8, 38, 100, 180, and 700 min, which correspond to the time for the first available prediction, prediction with the lowest MAPE, prediction with the highest MAPE, prediction with the highest temperature in the composite, and the fully cured composite, respectively. Overall, both models can predict the spatial temperature distribution and capture the temperature gradient at different time steps with less than 3.6% average MAPE, which occurs at about 100 min into the VARIM experiment, even when the temperature value changes greatly from as low as room temperature 25 °C, corresponding to the beginning of the VARIM process, to as high as 100 °C, which occurs after the epoxy resin has fully infused the glass fiber composite after an hour, and hit the highest chemical reaction point at around 180 min.

Based on the images, the high-temperature and low-temperature regions have evolved from the beginning to the end of the entire VARIM process. Since it is recognized that the uneven curing of the epoxy resin is the direct cause of the local buckling and other defects within the large glass fiber epoxy composite parts, the entire history of temperature change that reflects the experimental VARIM process can be divided into three phases based on the epoxy resin curing progress: the pre-curing period, which ends after the epoxy resin enters and infuses the entire dry glass fiber composite completely (at around 60 min); the drastic curing reaction period, which starts after the infusion finishes and ends when the elevated external heating is stopped (at around 350 min); and the post-curing period that starts after the external heating from the tabletop is fully stopped (at around 370 min). The

curing degree of the epoxy resin can be modeled as a function of temperature and time, as shown in Fig. 2 and explained in "A physics-based model for VARIM and composite curing processes" section. In the meantime, the epoxy resin curing process is accompanied by the release of heat that leads to a higher temperature in the composite, during which areas of heat concentration can also take shape. This positive interaction between the rising temperature and the accelerated curing makes the overall curing process spatially and temporally uneven, unstable, and unpredictable for composite manufacturers. Therefore, robust modeling tools capable of making fast and accurate temperature predictions are critical for manufacturers to make a timely decision to control and optimize the process. The proposed modeling tool based on RNN and LSTM models is aimed at accomplishing this goal.

The MAPE mapping helps evaluate the model prediction performance in different regions and times. It is observed from Fig. 17 that higher prediction error normally occurs at the temperature transition regions, especially at time steps when a rapid chemical reaction is happening that leads to the peak temperature during the curing process at around 180 min, as shown in Fig. 17c. It is worth noting that this peak temperature is purely due to epoxy resin curing, as the external heating is kept at 45 °C until around 200 min, as shown in Fig. 5. During the drastic curing reaction period from roughly 100 to 180 min, the temperature at the lower half of the image, which corresponds to the resin outlet, starts to increase dramatically from around 65-85 °C to around 100 °C. This is because the liquid epoxy resin is first infused into the system from the top and then accumulates inside the composite before being steadily discharged from the vacuum line at the resin outlet. Therefore, the curing degree of the fresh epoxy that enters from the inlet at the top lags greatly behind the epoxy resin that has a longer residence time inside the composite and a longer heating time by the



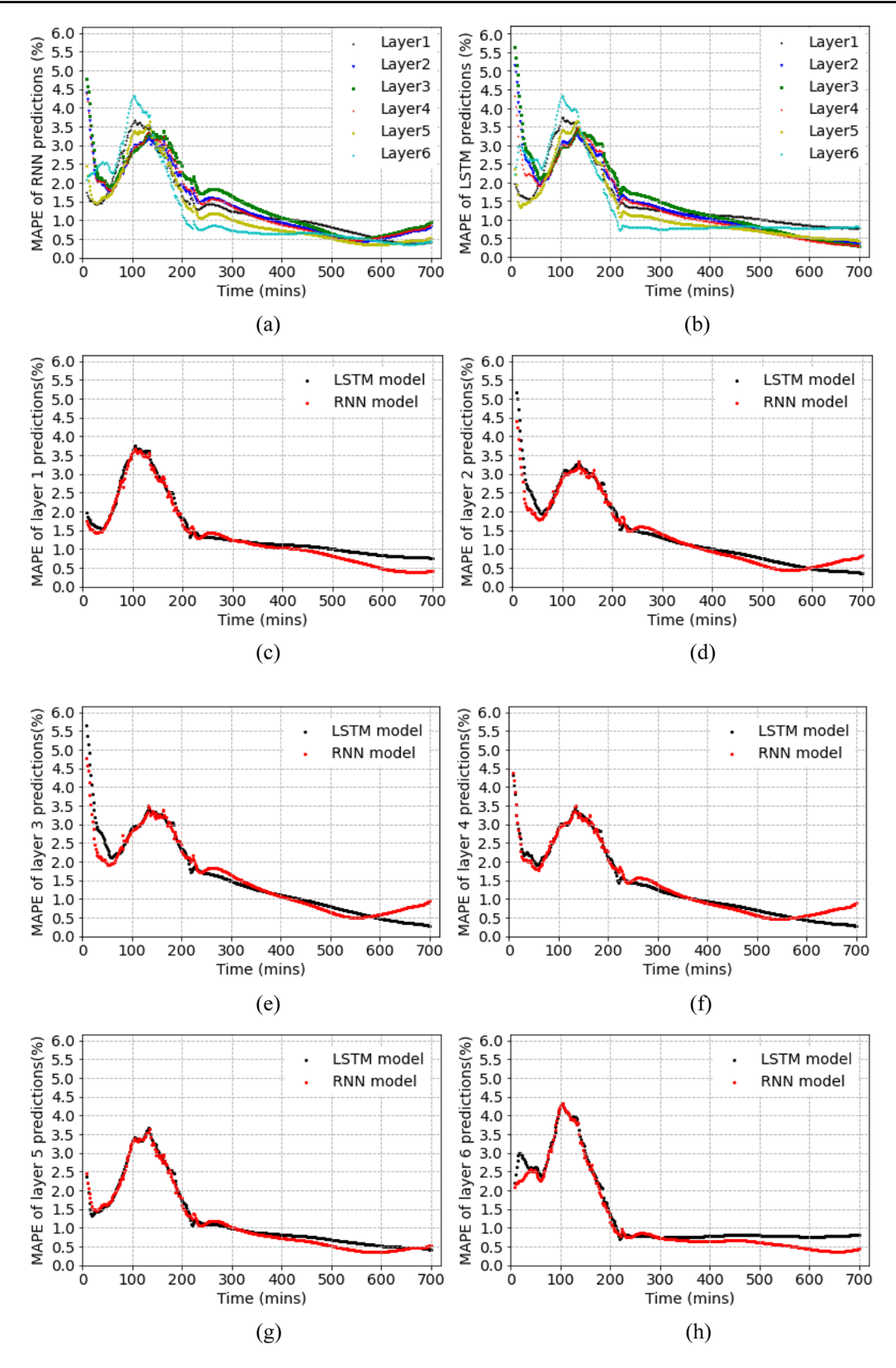


Fig. 16 Accuracy of temperature predictions of different layers of the composite at different time steps from trained ML models: **a** RNN predictions of all six layers; **b** LSTM predictions

of all six layers; ${\bf c}$ Comparison of predictions from RNN and LSTM models of layer 1, ${\bf d}$ layer 2, ${\bf e}$ layer 3, ${\bf f}$ layer 4, ${\bf g}$ layer 5, and ${\bf h}$ layer 6



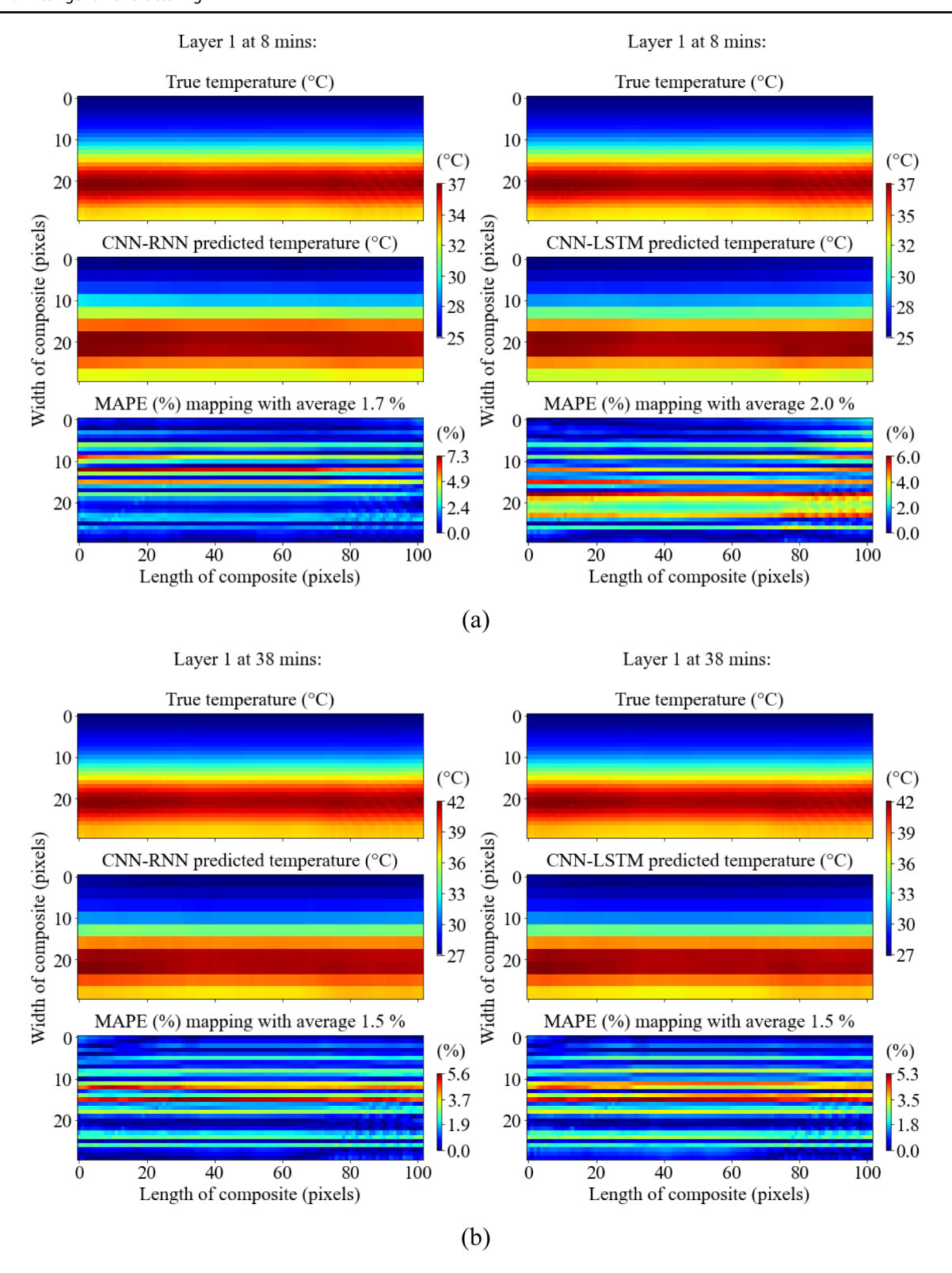
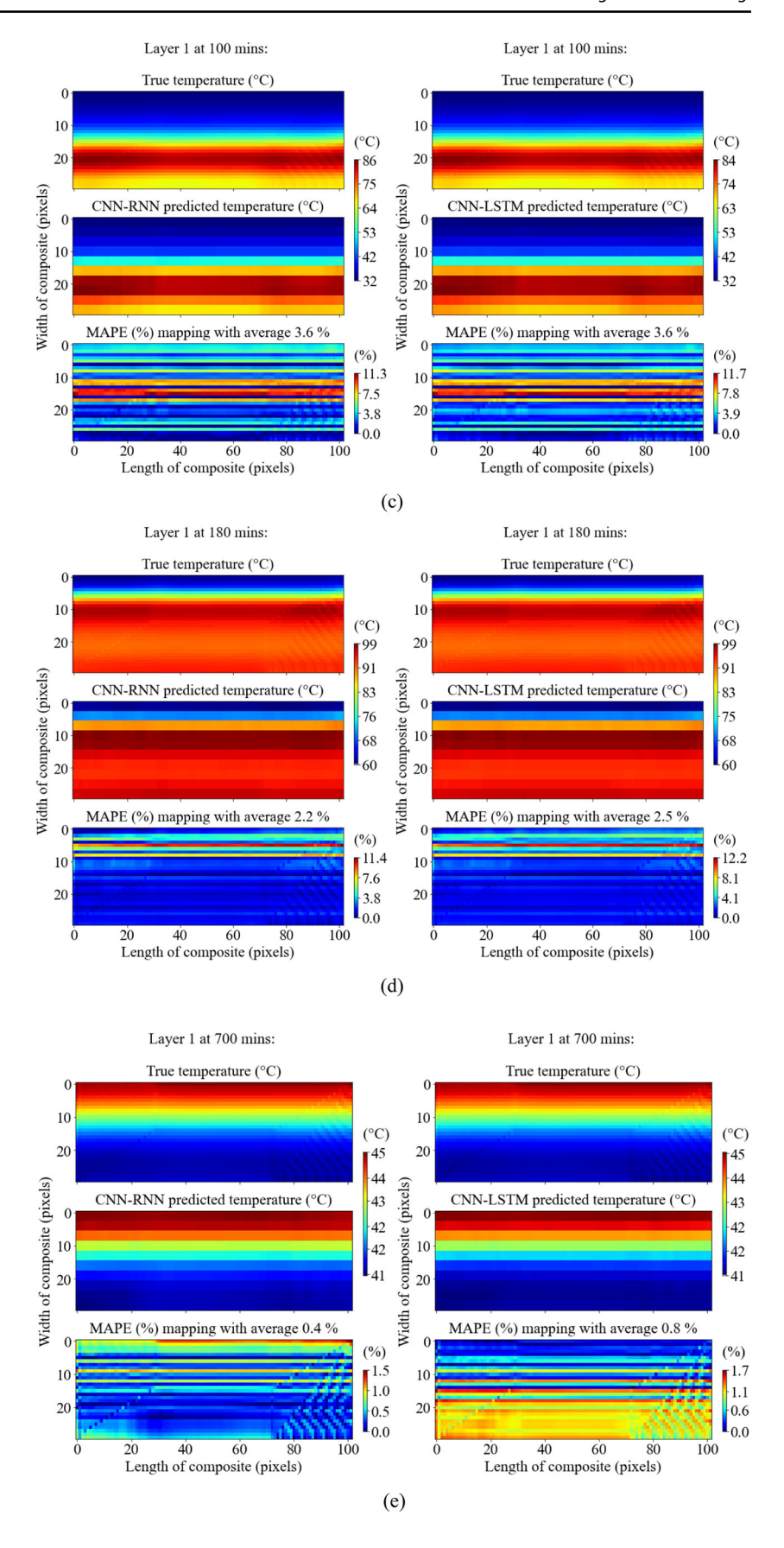


Fig. 17 The spatio-temporal temperature predictions from the CNN-RNN and CNN-LSTM models at a 8 min, b 38 min, c 100 min, d 180 min, and e 700 min



Fig. 17 continued





tabletop heater, as is observed in Fig. 17c and d, that the temperature at the resin inlet is only around 32 °C and 60 °C at 100 min and 180 min, respectively, while the temperature toward the outlet is about 84 °C and 100 °C, correspondingly. It is also during this period that the predictor has the highest local MAPE with more than 10% at the interfacial regions between the low and high-temperature regions, as shown by the contour maps in Fig. 17c and d, and also as observed from the MAPE vs. time step curves in Fig. 16. The large temperature difference is due to local heat concentration. Due to the small composite surface area $(2 \text{ m} \times 0.56 \text{ m})$, the heat generated from the epoxy resin in the curing process cannot be dissipated swiftly through the natural heat convection with the surrounding environment. The datasets with an image size of 102×30 pixels are too small to capture the large temperature difference within a small region, and provide enough pixel resolution for the CNN model to learn in order to extract the spatial feature as the convolutional filters with a size of 3×3 slides across the image during training. The high MAPE in these temperature transition regions, however, is fairly small, as indicated by the MAPE mapping and the low average MAPE, and therefore, it does not prevent the overall model from making reasonably accurate predictions and providing insights into the spatio-temporal temperature evolution for composite manufacturers.

To further evaluate the prediction results at different layers of the composite, the same temperature map and MAPE map for the mid and top layers at 100, 180, and 350 min are plotted in Fig. 18, with these time steps corresponding to the onset, the peak, and the end of the rapid epoxy resin curing phase, respectively, based on the temperature history plotted in Fig. 5. Predictions from the RNN model are selected due to its slightly better prediction accuracy than the LSTM model, based on the comparison of the results shown in Fig. 16. The RNN model has accurately captured the fact that the temperature in mid layer 3 is higher than the temperature of layer 6 at all time steps. This indicates that the model has learned and is capable of capturing the physics phenomenon that the heat tends to accumulate in the interior of the composite with its surfaces having a lower temperature due to the natural heat convection with the ambient. In addition, it is observed that the MAPE mappings at both the mid and top layers at all three selected time steps are very low, with the largest average MAPE value of 4.3%, as shown in Fig. 18a. The results indicate that the RNN model is capable of predicting the spatial temperature evolution during the VARIM process, including the rapid resin curing phase when the low and high-temperature regions on each layer shift dramatically. As the temperature value is a direct indication of the resin curing process, this ML-based model can potentially be used as one of the key criteria for composite manufacturers to monitor the temperature distribution in real-time during

manufacturing, so that the epoxy resin curing progress can be controlled to prevent the formation of defects.

Single temperature mapping prediction of the CNN-based model from processing parameters

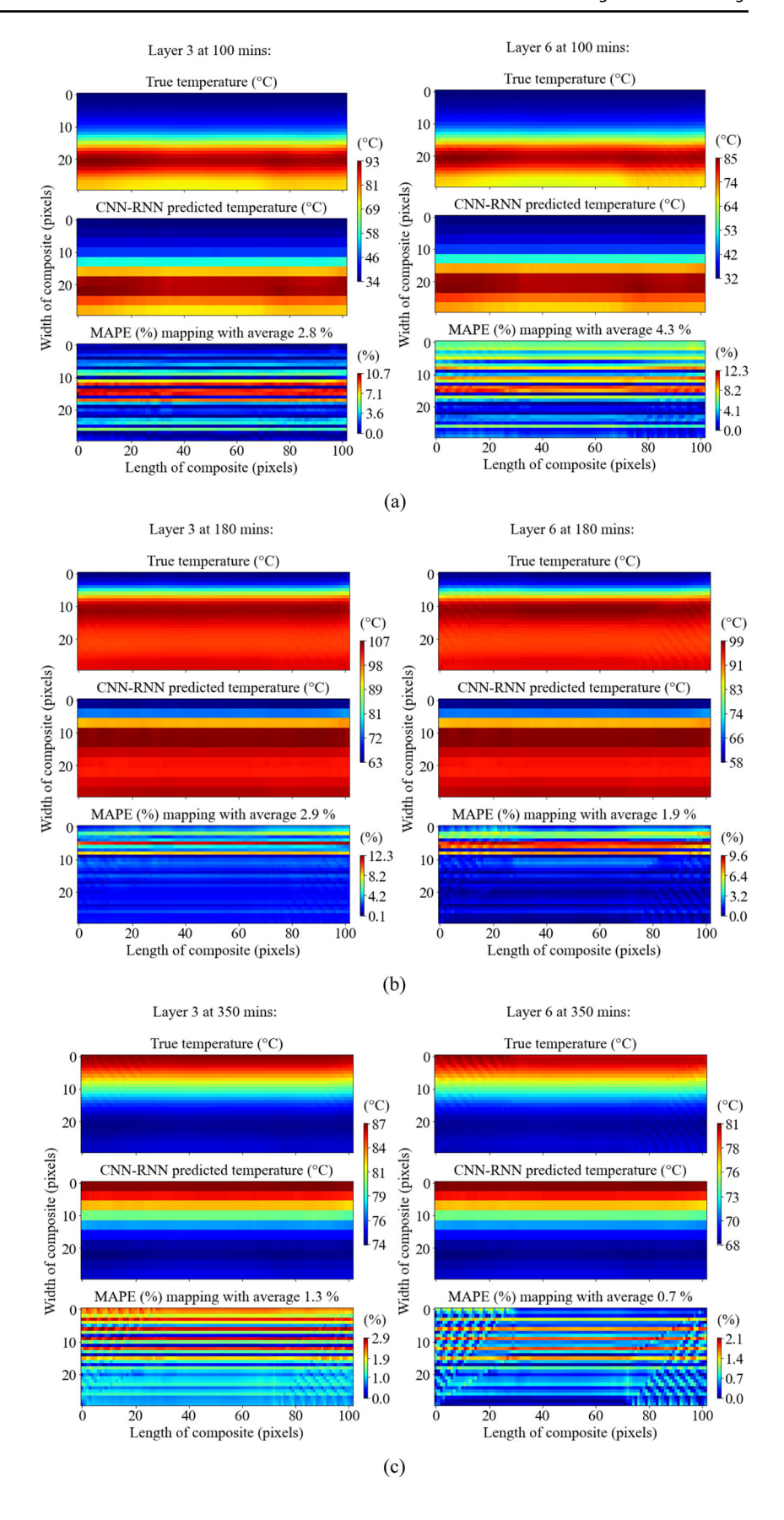
In addition to the CNN-RNN/LSTM-based spatio-temporal model, it is of interest to establish the direct linkage between the processing parameters and the corresponding temperature distribution resulting from them. As introduced in "A CNN-based model to link processing parameters to the temperature mapping" section, four temperature values and the layer height in the composite are the five processing parameters for the inputs of the CNN-based predictor whose structure is shown in Fig. 14b. Details of the model parameters are listed in Table 4. The model training history is presented in Fig. 19a, which shows good learning progress on the training and validation dataset with a size of 3000. Figure 19b shows the prediction results of the trained model on the separate testing dataset with a size of 750. The prediction accuracy is high with a MAPE value of less than 5% for 97.2% of all testing datasets, and an overall testing MAPE of 1.4% as shown in Table 4.

The effects of four external heating temperatures, T_1 , T₂, T₃, and T₄, and the prediction accuracy of the CNNbased model are visualized in Fig. 20, where the processing parameters and the corresponding temperature field at the mid section (layer 3) of the composite are provided. Overall, the trained CNN-based model shows good approximation capability by accurately predicting the 2D temperature field from a range of different input processing parameters, even when the temperature distribution, including the high and low-temperature regions, varies dramatically under different externally applied temperatures. Comparing the temperature fields shown in Fig. 20a and b, it is observed that the pre-heating temperature T₁ has a great influence on the temperature distribution after the primary epoxy curing is complete. With T₂ and T₃ both set at 83 °C, when T₁ is set at 41 °C, the highest temperature on layer 3 at 400 min is 49 °C, compared to that of 77 °C when T₁ is set at 46 °C. The low-temperature region at the resin inlet located on the top of the image in Fig. 20a indicates that if T_1 is set at 41 °C, the primary resin curing is somewhat incomplete at 400 min, as the high-temperature region has not yet transitioned from the outlet to the inlet in contrast to the high temperature at the inlet region at 400 min in Fig. 20b.

As illustrated in Fig. 14a, T_2 and T_3 are temperatures on the tabletop, representing the set temperature of the external heating source at the time approximately 250 min and 350 min into the VARIM experiment. T_1 , T_2 , T_3 , and T_4 are set to 45, 80, 80, and 20 °C, respectively, in the VARIM experiment in this study. By comparing results in Fig. 20c



Fig. 18 Comparison of the temperature predictions on the mid and top layers of the composite from the CNN-RNN model at the time a 100 min, b 180 min, and c 350 min





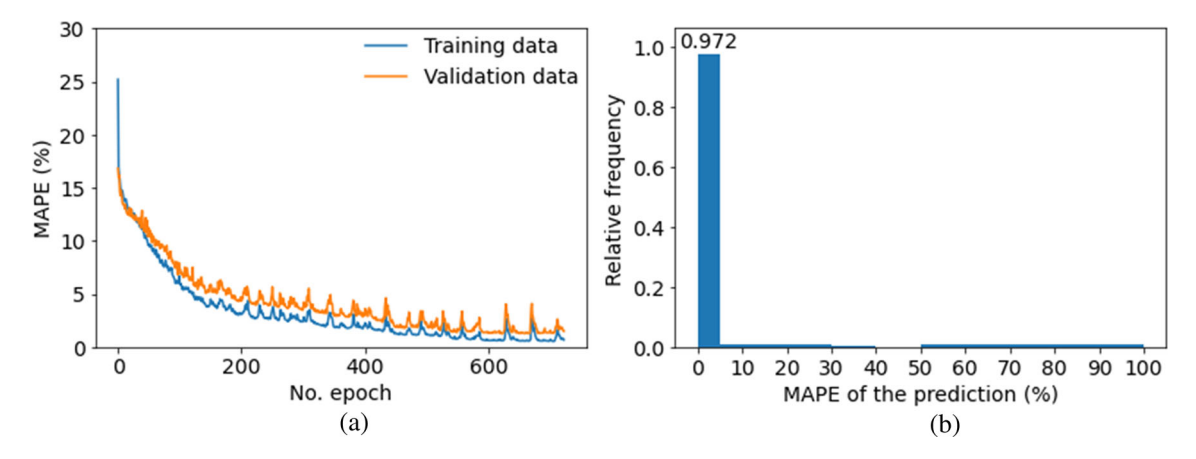


Fig. 19 a MAPE vs. training epoch (iteration) and b histogram of MAPE of prediction results from the trained CNN-based predictor on the testing dataset

and d, when $T_4 = 25~^{\circ}\text{C}$ is applied, a mere 1 $^{\circ}\text{C}$ increase in the temperature mapping of the entire layer 1 is observed, indicating the temperature T₄ does not affect the overall resin curing. This is because T₄ is the holding temperature starting at approximately 380 min, by which point the primary resin curing is finished, and therefore the heat release from the chemical reaction to the composite is small. In addition, the temperature distributions across the composite thickness are shown in Figs. 20d-f with the temperature range in color bars. It is observed that the overall temperature is the highest on the bottom layer 3, and the lowest on the top layer 6. This confirms the previous claim that the heat tends to accumulate in the interior of the composite, and that the temperature at the top surface is significantly lower due to the natural convection with the ambient. The CNN-based model provides temperature map predictions based on the five input parameters with over 95% accuracy; it also has captured the physics phenomenon, the direct correlation, and the high dependence of the temperature distribution on the externally applied temperature that assists in the resin curing process.

Conclusion

Based on developments in AI and smart manufacturing sectors, and with the purpose of fully capturing the complex mapping among the multiple physics-based models of the thermo-chemo-mechanical effects during the epoxy resin infusion and curing processes, in this study, a machine learning framework based on deep CNN and RNN/LSTM architecture has been established for fast prediction of the temperature distribution during the VARIM process. For training the CNN-RNN/LSTM-based ML model, a physics-based simulation tool is developed and validated through a

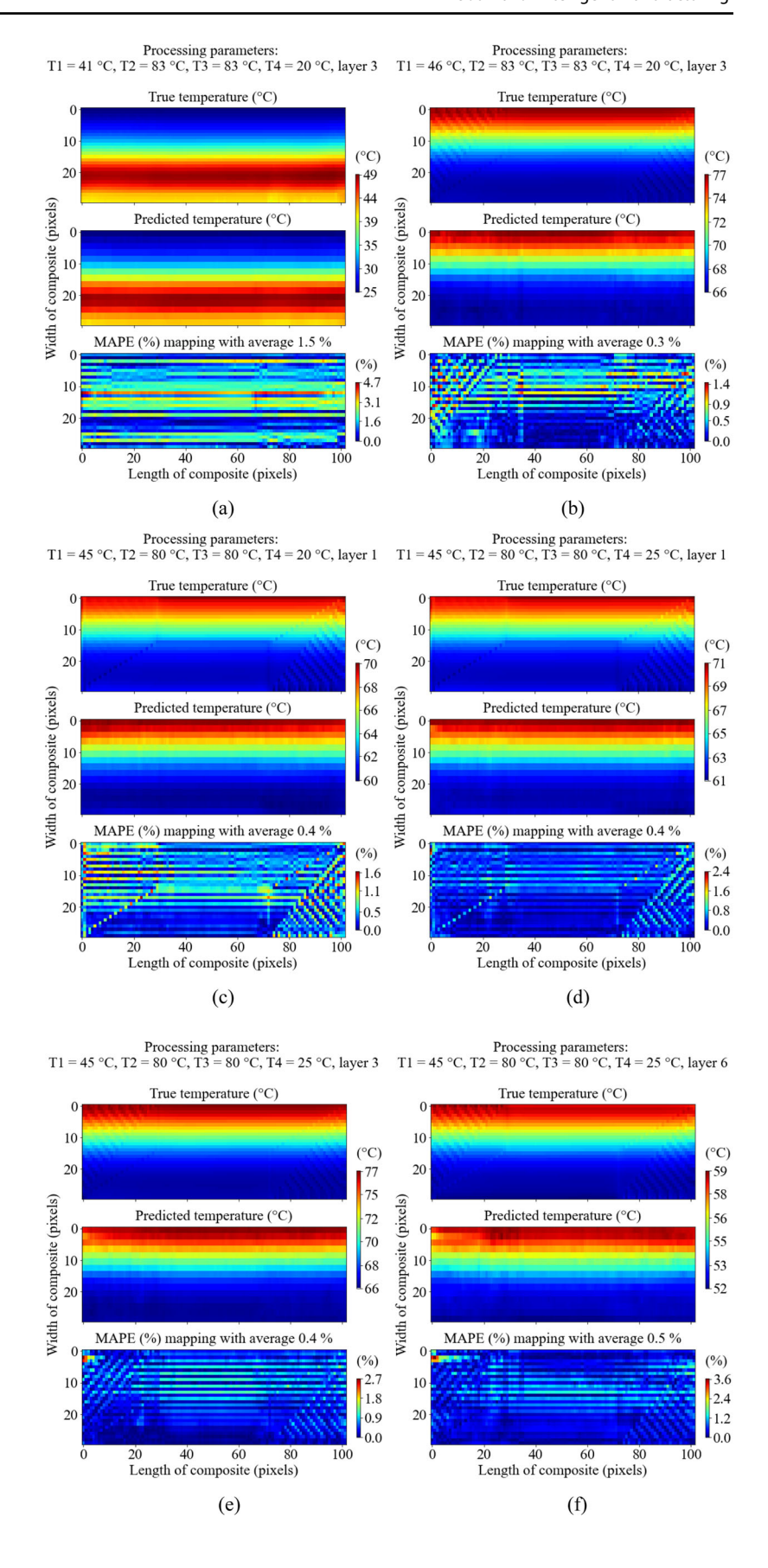
VARIM experiment before it is employed to generate the dataset needed for training the ML model. The physics-based model cannot be employed for real-time process control of the large blade manufacturing process due to lengthy computational time. The fully trained ML model can overcome this shortcoming; it is shown that it is capable of predicting spatiotemporal temperature distribution with an accuracy of > 94%, and is more than 100 times faster than the physics-based models. Trained on a single GPU, the ML-based model developed in this study is highly parallelizable and it is expected to maintain its fast and accurate prediction capabilities given the robust training process on much larger datasets.

In addition, five critical processing parameters of the VARIM process are designated, and linked to the single temperature mapping at the end of the resin curing process, using a similarly designed CNN-based model, so that it becomes feasible for manufacturers to quickly predict effects and ending results of key processing parameters, and therefore to make changes on the operating conditions frequently in real-time to get the desired and optimized temperature profile in the composite part at different curing phases. This model allows for extensive study and optimization of the process effects. As such, this work demonstrated the great potential of the proposed ML model as a digital twin of the VARIM process.

Future work will focus on integrating this framework with a closed-loop feedback system to adjust the processing parameters based on the prediction results. With more high-fidelity data available from both simulations and experiments, similar neural network models can be developed to account for more complicated VARIM processes and setup, and eventually be able to accurately predict the full-field temperature distribution on the full-scale wind turbine blade manufacturing process.



Fig. 20 Comparison of the temperature field prediction on different parts of the composite at 400 min from the CNN-based predictor with corresponding four key temperatures T₁, T₂, T₃, T₄, and the layer set at **a** 41 °C, 83 °C, 83 °C, 20 °C, layer 3; **b** 46 °C, 83 °C, 83 °C, 20 °C, layer 3; **c** 45 °C, 80 °C, 80 °C, 20 °C, layer 1; **d** 45 °C, 80 °C, 80 °C, 80 °C, 25 °C, layer 1; **e** 45 °C, 80 °C, 25 °C, layer 3; and **f** 45 °C, 80 °C, 80 °C, 25 °C, layer 6





Acknowledgements This paper is based upon work partially supported by the National Science Foundation under Grant Numbers 1362033 and 1916776 (I/UCRC for Wind Energy, Science, Technology, and Research) and from the members of WindSTAR I/UCRC. We also acknowledge the support of the Department of Energy, under Award Numbers DE-NA0003962 and DE-NA-0003525. We acknowledge Paul Ubrich, Mirna Robles, Nathan Bruno at Westlake Epoxy for helpful discussions. Lu also acknowledges the Louis A. Beecherl Jr. Chair for additional support. Any opinions, findings, and conclusions or recommendations expressed in this material are those of the authors and do not necessarily reflect the views of the National Science Foundation or the Department of Energy, or the sponsors. TPI Composites, Inc. is a composite manufacturer with a sector of business in the manufacturing of wind turbine blades, and a sponsoring company in the National Science Foundation (NSF) WindSTAR I/UCRC Center jointly operated between the University of Massachusetts at Lowell, and the University of Texas at Dallas. OlinTM EPOXY is a supplier and manufacturer of epoxy products, and a sponsoring company in the National Science Foundation (NSF) WindSTAR I/UCRC Center jointly operated between the University of Massachusetts at Lowell, and the University of Texas at Dallas. The partial support of UTD Wind is gratefully acknowledged.

Data availability Datasets, codes, and models used in this paper have been uploaded to GitHub as a reference for readers interested in performing additional analysis. Weblink to GitHub: https://github.com/Runyu-Zhang/Spatio-temporal-temperature-prediction-for-VARIM-process

Declarations

Conflict of interest The authors declare that they have no conflict of interest.

References

- Abadi, M., Agarwal, A., Barham, P., Brevdo, E., Chen, Z., Citro, C., et al. (2016). TensorFlow: Large-scale machine learning on heterogeneous distributed systems. arXiv. https://doi.org/10.48550/arxiv.1603.04467
- Abiodun, O. I., Jantan, A., Omolara, A. E., Dada, K. V., Mohamed, N. A. E., & Arshad, H. (2018). State-of-the-art in artificial neural network applications: A survey. *Heliyon*, 4(11), e00938. https://doi.org/10.1016/J.HELIYON.2018.E00938
- Albawi, S., Mohammed, T. A., & Al-Zawi, S. (2018). Understanding of a convolutional neural network. *Proceedings of 2017 Interna*tional Conference on Engineering and Technology, ICET 2017, 2018 pp. 1–6. https://doi.org/10.1109/ICENGTECHNOL.2017. 8308186
- Amini Niaki, S., Haghighat, E., Campbell, T., Poursartip, A., & Vaziri, R. (2021). Physics-informed neural network for modelling the thermochemical curing process of composite-tool systems during manufacture. Computer Methods in Applied Mechanics and Engineering, 384, 113959. https://doi.org/10.1016/J.CMA.2021. 113959
- Arnold, F., Demallie, I., Florence, L., & Kashinski, D. O. (2015). Method for collecting thermocouple data via secured shell over a wireless local area network in real time. *Review of Scientific Instruments*, 86(3), 035112. https://doi.org/10.1063/1.4915490
- Barari, B., Simacek, P., Yarlagadda, S., Crane, R. M., & Advani, S. G. (2019). Prediction of process-induced void formation in anisotropic Fiber-reinforced autoclave composite parts. *International Journal of Material Forming*, 13(1), 143–158. https://doi. org/10.1007/S12289-019-01477-4

- Bender, D., Schuster, J., & Heider, D. (2006). Flow rate control during vacuum-assisted resin transfer molding (VARTM) processing. *Composites Science and Technology*, 66(13), 2265–2271. https://doi.org/10.1016/J.COMPSCITECH.2005.12.008
- Chen, Y., Wang, Y., Dong, Z., Su, J., Han, Z., Zhou, D., et al. (2021). 2-D regional short-term wind speed forecast based on CNN-LSTM deep learning model. *Energy Conversion and Management*, 244, 114451. https://doi.org/10.1016/J.ENCONMAN.2021.114451
- Chiu, H. T., Yu, B., Chen, S. C., & Lee, L. J. (2000). Heat transfer during flow and resin reaction through fiber reinforcement. *Chemical Engineering Science*, 55(17), 3365–3376. https://doi.org/10.1016/S0009-2509(00)00004-X
- Cotrell, J., Musial, W., & Hughes, S. (2006). Necessity and requirements of a collaborative effort to develop a large wind turbine blade test facility in North America. https://doi.org/10.2172/882539
- Department of Energy (2022). Wind Turbines: the Bigger, the Better. https://www.energy.gov/eere/articles/wind-turbines-bigger-better
- Devillard, M., Hsiao, K. T., & Advani, S. G. (2005). Flow sensing and control strategies to address race-tracking disturbances in resin transfer molding—part II: Automation and validation. *Composites Part A: Applied Science and Manufacturing*, *36*(11), 1581–1589. https://doi.org/10.1016/J.COMPOSITESA.2004.04.009
- Devlin, J., Chang, M. W., Lee, K., & Toutanova, K. (2018). BERT: Pre-training of Deep Bidirectional Transformers for Language Understanding. NAACL HLT 2019 - 2019 Conference of the North American Chapter of the Association for Computational Linguistics: Human Language Technologies - Proceedings of the Conference, 1, pp. 4171–4186. https://doi.org/10.48550/arxiv. 1810.04805
- Djavadifar, A., Graham-Knight, J. B., Körber, M., Lasserre, P., & Najjaran, H. (2021). Automated visual detection of geometrical defects in composite manufacturing processes using deep convolutional neural networks. *Journal of Intelligent Manufacturing*. https://doi.org/10.1007/S10845-021-01776-1/TABLES/7
- Ersoy, N., & Tugutlu, M. (2010). Cure kinetics modeling and cure shrinkage behavior of a thermosetting composite. *Polymer Engineering & Science*, 50(1), 84–92. https://doi.org/10.1002/PEN. 21514
- Eum, S. H., Kageyama, K., Murayama, H., Uzawa, K., Ohsawa, I., Kanai, M., et al. (2007). Structural health monitoring using fiber optic distributed sensors for vacuum-assisted resin transfer molding. Smart Materials and Structures, 16(6), 2627. https://doi.org/ 10.1088/0964-1726/16/6/067
- Fu, Y., & Yao, X. (2022). A review on manufacturing defects and their detection of fiber reinforced resin matrix composites. *Composites Part C: Open Access*, 8, 100276. https://doi.org/10.1016/J. JCOMC.2022.100276
- Gers, F. A., Schmidhuber, J., & Cummins, F. (2000). Learning to forget: Continual prediction with LSTM. *Neural Computation*, *12*(10), 2451–2471. https://doi.org/10.1162/089976600300015015
- Gers, F. A., Schraudolph, N. N., & Schmidhuber, J. (2002). Learning precise timing with LSTM recurrent networks. *Journal of machine learning research*, 3(Aug), 115–143.
- Gokce, A., Chohra, M., Advani, S. G., & Walsh, S. M. (2005). Permeability estimation algorithm to simultaneously characterize the distribution media and the fabric preform in vacuum assisted resin transfer molding process. *Composites Science and Technology*, 65(14), 2129–2139. https://doi.org/10.1016/J.COMPSCITECH. 2005.05.012
- Goli, E., Vyas, S., Koric, S., Sobh, N., & Geubelle, P. H. (2020). ChemNet: A deep neural network for advanced composites manufacturing. *Journal of Physical Chemistry B*, 124(42), 9428–9437. https://doi.org/10.1021/ACS.JPCB.0C03328
- Goodfellow, I., Bengio, Y., & Courville, A. (2016). Deep learning. MIT press.



- Govignon, Q., Bickerton, S., & Kelly, P. A. (2008). Simulation of the complete resin infusion process. In 9th International Conference on Flow Processes in Composite Materials.
- Griffith, D. T., & Ashwill, T. D. (2011). The Sandia 100-meter all-glass baseline wind turbine blade: SNL100–00. Informe Técnico, Sandia National Laboratories.
- He, K., Chen, X., Xie, S., Li, Y., Dollár, P., & Girshick, R. (2022). Masked autoencoders are scalable vision learners. In Proceedings of the IEEE/CVF Conference on Computer Vision and Pattern Recognition (pp. 16000–16009).
- He, K., Zhang, X., Ren, S., & Sun, J. (2015). Deep Residual Learning for Image Recognition. Proceedings of the IEEE Computer Society Conference on Computer Vision and Pattern Recognition, 2016– December, 770–778. https://doi.org/10.48550/arxiv.1512.03385
- Hinton, G. E., Krizhevsky, A., & Wang, S. D. (2011). Transforming auto-encoders. In International conference on artificial neural networks. Springer, Berlin (pp. 44–51).
- Hinton, G. E., Osindero, S., & Teh, Y. W. (2006). A fast learning algorithm for deep belief nets. *Neural Computation*, *18*(7), 1527–1554. https://doi.org/10.1162/NECO.2006.18.7.1527
- Hochreiter, S. (2011). The vanishing gradient problem during learning recurrent neural nets and problem solutions. *International Journal* of Uncertainty, Fuzziness and Knowledge-Based Systems, 6(2), 107–116. https://doi.org/10.1142/S0218488598000094
- Hochreiter, S., & Schmidhuber, J. (1997). Long Short-Term Memory. Neural Computation, 9(8), 1735–1780. https://doi.org/10.1162/ NECO.1997.9.8.1735
- Hsiao, K.-T., & Heider, D. (2012). Vacuum assisted resin transfer molding (VARTM) in polymer matrix composites. *Manufactur-ing Techniques for Polymer Matrix Composites (PMCs)*. https://doi.org/10.1533/9780857096258.3.310
- Hsiao, K. T., Mathur, R., Advani, S. G., Gillespie, J. W., & Fink, B. K. (2000). A Closed Form Solution for Flow During the Vacuum Assisted Resin Transfer Molding Process. *Journal of Manufacturing Science and Engineering*, 122(3), 463–475. https://doi.org/10.1115/1.1285907
- Jain, A. K., Mao, J., & Mohiuddin, K. M. (1996). Artificial neural networks: A tutorial. *Computer*, 29(3), 31–44. https://doi.org/10. 1109/2.485891
- Jumper, J., Evans, R., Pritzel, A., Green, T., Figurnov, M., Ronneberger, O., et al. (2021). Highly accurate protein structure prediction with AlphaFold. *Nature*, 596(7873), 583–589. https://doi.org/10.1038/ s41586-021-03819-2
- Kaelbling, L. P., Littman, M. L., & Moore, A. W. (1996). Reinforcement Learning: A Survey. *Journal of Artificial Intelligence Research*, 4, 237–285. https://doi.org/10.1613/JAIR.301
- Kamal, M. R., & Ryan, M. E. (1980). The behavior of thermosetting compounds in injection molding cavities. *Polymer Engineer*ing & Science, 20(13), 859–867. https://doi.org/10.1002/PEN. 760201305
- Kamal, M. R., & Sourour, S. (1973). Kinetics and thermal characterization of thermoset cure. *Polymer Engineering & Science*, 13(1), 59–64. https://doi.org/10.1002/PEN.760130110
- Kedari, V. R., Farah, B. I., & Hsiao, K. T. (2011). Effects of vacuum pressure, inlet pressure, and mold temperature on the void content, volume fraction of polyester/e-glass fiber composites manufactured with VARTM process. *Journal of Composite Materials*, 45(26), 2727–2742. https://doi.org/10.1177/0021998311415442
- Kingma, D. P., & Ba, J. L. (2014). Adam: A Method for Stochastic Optimization. 3rd International Conference on Learning Representations, ICLR 2015 - Conference Track Proceedings. https:// doi.org/10.48550/arxiv.1412.6980
- Kingma, D. P., & Welling, M. (2019). An Introduction to Variational Autoencoders. *Foundations and Trends® in Machine Learning*, 12(4), 307–392. https://doi.org/10.1561/2200000056

- Kravchenko, O. G., Li, C., Strachan, A., Kravchenko, S. G., & Pipes, R. B. (2014). Prediction of the chemical and thermal shrinkage in a thermoset polymer. *Composites Part a: Applied Science and Manufacturing*, 66, 35–43. https://doi.org/10.1016/J. COMPOSITESA.2014.07.002
- Krizhevsky, A., Sutskever, I., & Hinton, G. E. (2017). Imagenet classification with deep convolutional neural networks. *Communications* of the ACM, 60(6), 84–90.
- Krogh, A. (2008). What are artificial neural networks? *Nature Biotechnology*, 26(2), 195–197. https://doi.org/10.1038/nbt1386
- Kusiak, A. (2017). Smart manufacturing must embrace big data (pp. 23–25). Taylor & Francis.
- Kusiak, A. (2017). Smart manufacturing (pp. 508–517). Taylor & Francis
- Lecun, Y., Bengio, Y., & Hinton, G. (2015). Deep learning. *Nature*, 521(7553), 436–444. https://doi.org/10.1038/nature14539
- Lipton, Z. C., Berkowitz, J., & Elkan, C. (2015). A Critical review of recurrent neural networks for sequence learning. arXiv. https://doi. org/10.48550/arxiv.1506.00019
- Liu, C., Zhu, H., Tang, D., Nie, Q., Li, S., Zhang, Y., & Liu, X. (2022). A transfer learning CNN-LSTM network-based production progress prediction approach in IIoT-enabled manufacturing.https://doi. org/10.1080/00207543.2022.2056860
- Ma, L., Athreya, S. R., Mehta, R., Barpanda, D., & Shafi, A. (2017). Numerical modeling and experimental validation of nonisothermal resin infusion and cure processes in large composites. *Journal of Reinforced Plastics and Composites*, 36(10), 780–794. https://doi. org/10.1177/0731684417691673
- Mal, O., Couniot, A., & Dupret, F. (1998). Non-isothermal simulation of the resin transfer moulding press. *Composites Part A: Applied Science and Manufacturing*, 29(1–2), 189–198. https://doi.org/10.1016/S1359-835X(97)00065-1
- Mathuw, R., Advani, S. G., Heider, D., Hoffmann, C., Gillespie, J. W., & Fink, B. K. (2001). Flow front measurements and model validation in the vacuum assisted resin transfer molding process. *Polymer Composites*, 22(4), 477–490. https://doi.org/10.1002/PC. 10553
- Matsuzaki, R., Kobayashi, S., Todoroki, A., & Mizutani, Y. (2011).
 Control of resin flow/temperature using multifunctional interdigital electrode array film during a VaRTM process. *Composites Part A: Applied Science and Manufacturing*, 42(7), 782–793. https://doi.org/10.1016/J.COMPOSITESA.2011.03.004
- Matsuzaki, R., Kobayashi, S., Todoroki, A., & Mizutani, Y. (2013).
 Flow control by progressive forecasting using numerical simulation during vacuum-assisted resin transfer molding. *Composites Part A: Applied Science and Manufacturing*, 45, 79–87. https://doi.org/10.1016/J.COMPOSITESA.2012.09.014
- Meng, M., Chua, Y. J., Wouterson, E., & Ong, C. P. K. (2017). Ultrasonic signal classification and imaging system for composite materials via deep convolutional neural networks. *Neurocomputing*, 257, 128–135. https://doi.org/10.1016/J.NEUCOM.2016.11.066
- Mnih, V., Kavukcuoglu, K., Silver, D., Graves, A., Antonoglou, I., Wierstra, D., & Riedmiller, M. (2013). Playing Atari with Deep Reinforcement Learning. https://doi.org/10.48550/arxiv.1312.5602
- Nalla, A. R., Fuqua, M., Glancey, J., & Lelievre, B. (2007). A multi-segment injection line and real-time adaptive, model-based controller for vacuum assisted resin transfer molding. *Composites Part A: Applied Science and Manufacturing*, 38(3), 1058–1069. https://doi.org/10.1016/J.COMPOSITESA.2006.06.021
- Nicolay, P., Matloub, R., Bardong, J., Mazzalai, A., & Muralt, P. (2017).
 A concept of wireless and passive very-high temperature sensor.
 Applied Physics Letters, 110(18), 184104. https://doi.org/10.1063/1.4983085



- Nielsen, D. R., & Pitchumani, R. (2002). Closed-loop flow control in resin transfer molding using real-time numerical process simulations. *Composites Science and Technology*, 62(2), 283–298. https:// doi.org/10.1016/S0266-3538(01)00213-5
- Olah, C. (2015). Understanding lstm networks. https://colah.github.io/ OpenAI. (2022). https://openai.com/
- Ouahbi, T., Saouab, A., Bréard, J., Ouagne, P., & Chatel, S. (2007). Modelling of hydro-mechanical coupling in infusion processes. *Composites Part a: Applied Science and Manufacturing*, 38(7), 1646–1654. https://doi.org/10.1016/J.COMPOSITESA. 2007.03.002
- Pathak, D., Krahenbuhl, P., Donahue, J., Darrell, T., Efros, A. A. (2016). Context encoders: Feature learning by inpainting. In Proceedings of the IEEE conference on computer vision and pattern recognition (pp. 2536–2544).
- Pfrommer, J., Zimmerling, C., Liu, J., Kärger, L., Henning, F., & Beyerer, J. (2018). Optimisation of manufacturing process parameters using deep neural networks as surrogate models. *Procedia CIRP*, 72, 426–431. https://doi.org/10.1016/J.PROCIR.2018.03.046
- Potter, K. D. (2009). Understanding the origins of defects and variability in composites manufacture. In International conference on composite materials (ICCM)-17, Edinburgh (p. 18).
- Ramesh, A., Pavlov, M., Goh, G., Gray, S., Voss, C., Radford, A., ... & Sutskever, I. (2021). Zero-shot text-to-image generation. In International Conference on Machine Learning. PMLR (pp. 8821–8831)
- Reed, S., Zolna, K., Parisotto, E., Colmenarejo, S. G., Novikov, A., Barth-Maron, G., ..., de Freitas, N. (2022). A generalist agent. arXiv preprint arXiv:2205.06175.
- Rumelhart, D. E., Hinton, G. E., & Williams, R. J. (1985). *Learning internal representations by error propagation*. California Univ San Diego La Jolla Inst for Cognitive Science.
- Rumelhart, D. E., Hinton, G. E., & Williams, R. J. (1986). Learning representations by back-propagating errors. *Nature*, *323*(6088), 533–536. https://doi.org/10.1038/323533a0
- Samborsky, D. D., Agastra, P., & Mandell, J. F. (2010). Fatigue trends for wind blade infusion resins and fabrics. Collection of Technical Papers - AIAA/ASME/ASCE/AHS/ASC Structures, Structural Dynamics and Materials Conference. https://doi.org/10.2514/6. 2010-2820
- Sharma, A., Vans, E., Shigemizu, D., Boroevich, K. A., & Tsunoda, T. (2019). DeepInsight: A methodology to transform a non-image data to an image for convolution neural network architecture. Scientific Reports, 9(1), 1–7. https://doi.org/10.1038/s41598-019-47765-6
- Shojaei, A., Ghaffarian, S. R., & Karimian, S. M. H. (2003). Modeling and simulation approaches in the resin transfer molding process: A review. *Polymer Composites*, 24(4), 525–544. https://doi.org/ 10.1002/PC.10050
- Siddig, N. A., Binetruy, C., Syerko, E., Simacek, P., & Advani, S. (2018). A new methodology for race-tracking detection and criticality in resin transfer molding process using pressure sensors. *Journal of Composite Materials*, 52(29), 4087–4103.
- Silver, D., Huang, A., Maddison, C. J., Guez, A., Sifre, L., van den Driessche, G., et al. (2016). Mastering the game of Go with deep neural networks and tree search. *Nature*, 529(7587), 484–489. https://doi.org/10.1038/nature16961
- Silver, D., Schrittwieser, J., Simonyan, K., Antonoglou, I., Huang, A., Guez, A., et al. (2017). Mastering the game of Go without human knowledge. *Nature*, 550(7676), 354–359. https://doi.org/10.1038/ nature24270
- Simacek, P., Eksik, Ö., Heider, D., Gillespie, J. W., & Advani, S. (2012). Experimental validation of post-filling flow in vacuum assisted resin transfer molding processes. *Composites Part A: Applied Science and Manufacturing*, 43(3), 370–380. https://doi.org/10.1016/ J.COMPOSITESA.2011.10.002

- Simacek, P., Heider, D., Gillespie, J. W., & Advani, S. (2009). Post-filling flow in vacuum assisted resin transfer molding processes: Theoretical analysis. *Composites Part A: Applied Science and Manufacturing*, 40(6–7), 913–924. https://doi.org/10.1016/J.COMPOSITESA.2009.04.018
- Simonyan, K., & Zisserman, A. (2014). Very deep convolutional networks for large-scale image recognition. 3rd International Conference on Learning Representations, ICLR 2015 - Conference Track Proceedings. https://doi.org/10.48550/arxiv.1409.1556
- Struzziero, G., & Teuwen, J. J. E. (2019). Effect of convection coefficient and thickness on optimal cure cycles for the manufacturing of wind turbine components using VARTM. Composites Part a: Applied Science and Manufacturing, 123, 25–36. https://doi.org/10.1016/J.COMPOSITESA.2019.04.024
- Sun, X., Li, S., & Lee, L. J. (1998). Mold filling analysis in vacuumassisted resin transfer molding. Part I: SCRIMP based on a highpermeable medium. *Polymer Composites*, 19(6), 807–817. https:// doi.org/10.1002/PC.10155
- Sutton, R. S., & Barto, A. G. (2018). Reinforcement learning: An introduction. MIT press.
- Szarski, M., & Chauhan, S. (2023). Instant flow distribution network optimization in liquid composite molding using deep reinforcement learning. *Journal of Intelligent Manufacturing*, 34(1), 197–218
- Tao, F., Qi, Q., Liu, A., & Kusiak, A. (2018). Data-driven smart manufacturing. *Journal of Manufacturing Systems*, 48, 157–169. https://doi.org/10.1016/J.JMSY.2018.01.006
- Tifkitsis, K. I., & Skordos, A. A. (2020). Real time uncertainty estimation in filling stage of resin transfer molding process. *Poly*mer Composites, 41(12), 5387–5402. https://doi.org/10.1002/PC. 25803
- Upadhyaya, P., Roy, S., Haque, M. H., & Lu, H. (2013). A novel numerical–experimental approach for predicting delamination in high temperature polymer matrix composites. *Composite Structures*, 104, 118–124. https://doi.org/10.1016/J.COMPSTRUCT. 2013.04.008
- Vincent, P., Larochelle, H., Lajoie, I., Bengio, Y., & Manzagol, P.-A. (2010). Stacked denoising autoencoders: Learning useful representations in a deep network with a local denoising criterion. *The Journal of Machine Learning Research*. https://doi.org/10.5555/1756006.1953039
- Wisnom, M. R., Gigliotti, M., Ersoy, N., Campbell, M., & Potter, K. D. (2006). Mechanisms generating residual stresses and distortion during manufacture of polymer–matrix composite structures. *Composites Part A: Applied Science and Manufacturing*, 37(4), 522–529. https://doi.org/10.1016/J.COMPOSITESA.2005.05.019
- Wurman, P. R., Barrett, S., Kawamoto, K., MacGlashan, J., Subramanian, K., Walsh, T. J., et al. (2022). Outracing champion gran turismo drivers with deep reinforcement learning. *Nature*, 602(7896), 223–228. https://doi.org/10.1038/s41586-021-04357-7
- Yun, M.-Y., Lopez, E., Chinesta, F., & Advani, S. (2018). Manifold embedding of heterogeneity in permeability of a woven fabric for optimization of the VARTM process. *Composites Science and Technology*, 168, 238–245. https://doi.org/10.1016/J.COMPSCITECH.2018.10.006
- Zhang, R., Li, W., Jiao, Y., Paniagua, C., Ren, Y., & Lu, H. (2023). Porosity evolution under increasing tension in wire-arc additively manufactured aluminum using in-situ micro-computed tomography and convolutional neural network. *Scripta Materialia*, 225, 115172. https://doi.org/10.1016/J.SCRIPTAMAT.2022.115172



- Zhang, Z., & Friedrich, K. (2003). Artificial neural networks applied to polymer composites: A review. *Composites Science and Technology*, 63(14), 2029–2044. https://doi.org/10.1016/S0266-3538(03)00106-4
- Zhongliang, M., Le, Q., Wei, H., & Liming, H. (2019). A novel approach on the study of cure kinetics for rheological isothermal and non-isothermal methods. *Composites Part B: Engineering*, 162, 242–249. https://doi.org/10.1016/J.COMPOSITESB.2018.10.066
- Zhou, K., Sun, H., Enos, R., Zhang, D., & Tang, J. (2021). Harnessing deep learning for physics-informed prediction of composite strength with microstructural uncertainties. *Computational Materials Science*, 197, 110663. https://doi.org/10.1016/J. COMMATSCI.2021.110663
- Zhu, Y., Brettin, T., Xia, F., Partin, A., Shukla, M., Yoo, H., et al. (2021). Converting tabular data into images for deep learning with convolutional neural networks. *Scientific Reports*, 11(1), 1–11. https://doi.org/10.1038/s41598-021-90923-y

Publisher's Note Springer Nature remains neutral with regard to jurisdictional claims in published maps and institutional affiliations.

Springer Nature or its licensor (e.g. a society or other partner) holds exclusive rights to this article under a publishing agreement with the author(s) or other rightsholder(s); author self-archiving of the accepted manuscript version of this article is solely governed by the terms of such publishing agreement and applicable law.

